Research Article

Hooman Barati Sedeh, Mohammad Mahdi Salary and Hossein Mosallaei*

# Time-varying optical vortices enabled by time-modulated metasurfaces

https://doi.org/10.1515/nanoph-2020-0202
Received March 17, 2020; accepted May 20, 2020

**Abstract:** In this paper, generation of optical vortices with time-varying orbital angular momentum (OAM) and topological charge is theoretically demonstrated based on time-modulated metasurfaces with a linearly azimuthal frequency gradient. The topological charge of such dynamic structured light beams is shown to continuously and periodically change with time evolution while possessing a linear dependence on time and azimuthal frequency offset. The temporal variation of OAM yields a self-torqued beam exhibiting a continuous angular acceleration of light. The phenomenon is attributed to the azimuthal phase gradient in space-time generated by virtue of the spatiotemporal coherent path in the interference between different frequencies. In order to numerically authenticate this newly introduced concept, a reflective dielectric metasurface is modelled consisting of silicon nanodisk heterostructures integrated with indium-tin-oxide and gate dielectric layers on top of a mirror-backed silicon slab which renders an electrically tunable guided mode resonance mirror in near-infrared regime. The metasurface is divided into several azimuthal sections wherein nanodisk heterostructures are interconnected via nanobars serving as biasing lines. Addressing azimuthal sections with radio-frequency biasing signals of different frequencies, the direct dynamic photonic transitions of leaky-guided modes are leveraged for realization of an azimuthal frequency gradient in the optical field. Generation of dynamic twisted light beams with time-varying OAM by the metasurface is verified via performing several numerical simulations. Moreover, the role of modulation waveform and frequency gradient on the temporal evolution and diversity of generated optical vortices is investigated which offer a robust electrical control over the number of dynamic beams and their degree of self-torque. Our results point toward a new class of structured light for time-division multiple access in optical and quantum communication systems as well as unprecedented optomechanical manipulation of objects.

**Keywords:** orbital angular momentum; optical vortex beam; time-modulated metasurface.

## 1 Introduction

A light beam has two different forms of momenta, namely linear and angular momenta. While the former is obtained from $\mathbf{P}=\hbar\mathrm{k}$ , with $\hbar$ being the reduced Planck's constant and k being the wave vector, the latter can be decomposed into two distinct contributions of spin angular momentum (SAM) and orbital angular momentum (OAM) [1]. SAM is directly related to the polarization of a light beam and can get two values of $+\hbar$ $(-\hbar)$ for right (left) handed circular polarization. On the other hand, OAM is associated with a helical or twisted wavefront of a structured light beam and can take discrete unbounded values of $\mathbf{L}=l\hbar$, with $l$ being an integer (i.e., $l \in \mathbb{Z}$) defining the number of phase windings per wavelength which is referred to as topological quantum number or topological charge (used for quantized topological invariant quantities). The high-dimensionality of Hilbert space consisting of OAM modes and mutual orthogonality of distinct OAM states make them applicable for a wide range of applications [2] such as optical communications with enhanced capacity [3, 4], optical tweezers [5, 6], super-resolution microscopy [7, 8], and quantum entanglement [9, 10]. Several methods have been proposed to generate OAM-carrying beams [11], including spiral phase plates (SPP) [12–14], holographic diffraction gratings [15, 16], angular grating [17, 18], trench waveguides [19] and transformation optics [20].

Optical vortices (OVs) are a generic class of OAM-carrying structured light beams which possess an

*Corresponding author: Hossein Mosallaei, Metamaterials Lab, Electrical and Computer Engineering Department, Northeastern University, Boston, MA, 02115, USA, E-mail: hosseinm@ece.neu.edu
Hooman Barati Sedeh and Mohammad Mahdi Salary: Metamaterials Lab, Electrical and Computer Engineering Department, Northeastern University, Boston, MA, 02115, USA. https://orcid.org/0000-0002-3908-6652 (H. Barati Sedeh). https://orcid.org/0000-0003-2056-3348 (M.M. Salary)

azimuthal phase dependence of $\exp(il\varphi)$ wherein $l$ defines topological charge. As shown in the seminal work of Allen et al. [21], the optical field of these beams exhibits a topological phase singularity along the beam axis which leads to a vanished intensity. As a result, the intensity pattern of an OV beam shows a dark central spot in its cross-section, whose radius increases by increasing the value of topological charge. Spatiotemporal optical vortices (STOV) have been recently introduced as a new class of OAM-carrying light beams whose topological charge has a space-time dependence [22, 23]. These beams can physically exist if one could satisfy the condition of non-collinearity between intrinsic OAM and linear momentum, which is $\mathbf{L} \nparallel \mathbf{P}$. In particular, it is shown that the collinearity of $\mathbf{P}$ and $\mathbf{L}$ will be broken upon the Lorentz transformation because the momentum is transformed as a vector, while the OAM is transformed as a part of the antisymmetric angular-momentum tensor. STOVs have gained the attention of the scientific community due to their importance in both theoretical and practical studies such as in describing the particle collisions [24], optics of moving media [25, 26] and quantum communications [27]. Several works have been conducted to generate STOVs whose topological charge has a spatial dependency along the propagation direction [28–30]. Such vortices are of particular interest for (de)acceleration of the structured light. A common approach used for this purpose is to superimpose two structured light beams with opposite topological charges and slightly different wave vectors. As a result, the obtained beam after superposition possesses rotating behavior while exhibiting angular velocity and radial acceleration [29]. It should be mentioned that although the generated beam will possess different topological charges at different locations, yet the beam would appear "static" at any instant of time. That is, in a specific position of space, the radius of the vortex remains unchanged as time goes on.

Therefore, according to the above-mentioned points, it could be understood that another added layer of complexity in this field of research would be the generation and propagation of a "dynamic" spatiotemporal beam whose topological charge varies with respect to time (i.e., $l(t)$) as it propagates through the space. To the authors' best knowledge, the hidden physics behind such kind of dynamic optical vortices had remained unexplored until 2019 by the pioneering work of Rego et al. [31]. As it has been reported in this work, generating a time-varying OAM beam is possible by employing two time-delayed, collinear and linearly polarized infrared pulses possessing different topological charges of $l_1$ and $l_2$ but at the same wavelength, which are focused into an argon gas acting as a high harmonic generation (HHG) medium. The result of such a nonlinear process is a pulse whose topological charge is varying with respect to time along the pulse while being bounded between two values of $l_1$ and $l_2$ (i.e., $l_1 < l(t) < l_2$). The angular momentum of the generated light will consequently be a function of time since $L(t) = l(t)\hbar$. This will, in turn, cause the light to carry a constant optical torque ($\tau = dL/dt$). This torque is referred to as "self-torque" to be distinguished from the mechanical torque exerted on a scatterer by static OAM-carrying light beams in that it remains an inherent property of the light beam as it propagates in free-space after being generated in the absence of any external agent [31]. Such dynamic torqued light beam could potentially be used in numerous applications such as in optical tweezers [6, 32–34], attosecond pulses [35] and fundamental studies of Bose–Einstein condensates [36]. The underlying operating principle of such a time-dependent OAM pulse can be attributed to the azimuthal frequency chirp imparted on the radiation emission at the microscopic scale due to the coherent properties of HHG. It should be noted that due to nonlinearity of HHG process, this approach requires high intensity excitation. Moreover, tuning the degree of self-torque requires control over the time-delay and duration of two driving pulses which requires bulky optical components with precise alignments. In this paper, we aim at introducing an alternative approach for generation of time-varying optical vortices which relies on imparting an azimuthal frequency gradient on the wavefront of light at the macroscopic level via a linear time-modulated metasurface offering intensity-independent operation and robust electrical tunability of the self-torque.

Metasurfaces, planar two-dimensional arrays of sub-wavelength unit cells, have been a subject of intense research over the last decade by virtue of offering an unprecedent capability in engineering the wavefront of light by imparting abrupt resonant or geometric phase shifts to the scattered light [37, 38]. The compact footprint and ease of fabrication make metasurfaces ideal candidates for developing flat optical components integrated into on-chip devices. Moreover, metasurface-based optical components yield a great potential for enabling novel functionalities and/or outperforming their conventional bulky counterparts in terms of efficiency. Owing to the remarkable advantages offered by metasurfaces, they have been widely used as a mean of generating OAM-carrying light beams for different purposes including optical communication [39–41]. However, despite these expeditious growths in metasurface-based concepts both in theoretical and practical aspects, a main drawback of static metasurfaces is their fixed functionality. That is, their

optical characteristics and response are set in stone after they have been designed and cannot be changed afterward. This tantalizing characteristic of passive metasurfaces has led to new research on actively controllable metasurfaces that allow for real-time control over the wavefront of light by controlling an external stimulus [42–45]. The constituent elements of such active metasurfaces can also be modulated in time under application of a time-varying external stimulus, rendering a space-time varying surface which allows for extending the concepts of electromagnetic scattering in spatiotemporally modulated media [46] into the realm of metasurfaces. This has led to the emergence of time-modulated metasurfaces (TMMs) as a new paradigm for light manipulation enabling a myriad of new physical phenomena and further broadening the range of possible applications of metasurfaces [47–49].

It has been shown that introducing a space-time phase gradient in a TMM can break the Lorentz reciprocity and time-reversal symmetry [50–55]. Space-time coding has also been recently adopted to develop digital metasurfaces capable of light manipulation in space and frequency while offering nonreciprocity [56–59]. In addition to nonreciprocity, TMMs hold a great potential for a wide range of applications such as wavefront engineering [60–63], extreme energy accumulation [64], spectral camouflaging [65, 66], wide band impedance matching [67, 68], signal amplification [69], pulse shaping [70–72], and providing multiple access through multiplexing and multicasting [73, 74]. A fundamental property of a TMM is frequency mixing which leads to conversion of an incident frequency ($f_0$) into higher-order frequency harmonics. This allows for control over the spectral content of light as well as its spatial characteristics. In particular, the control over the frequency of scattered light can be used for generation of a frequency gradient which translates into a spatiotemporal phase gradient and enables generation of dynamic spatiotemporal light beams evolving in space-time at the steady-state [75, 76]. Such a phenomenon has been initially proposed in the framework of frequency diverse array (FDA) in conventional radiating antennas [77]. Unlike phased array antennas employing a progressive phase shift in feeding the radiating elements of an array antenna, FDAs apply a progressive frequency offsets in feeding the radiating elements of an array antenna which results in a periodic range- and time-dependent directive beam pattern continuously scanning the space at the steady-state. While the concept of FDA radars is well-established in the realm of radio-frequency (RF) antennas [78], it has been recently extended to the realm of metasurfaces as a new approach for ultrafast beam-scanning with wide angle-of-view for light detection and range (LiDAR). For this purpose, Shaltout et al. [79] have proposed a passive metasurface which can focus different frequencies into distinct focal spots at a focal plane under illumination of a frequency-comb source which renders a virtual frequency array leading to ultrafast spatiotemporal beam scanning. It has also been demonstrated that TMMs can be used for this purpose by varying the modulation frequency of their constituent elements with a progressive offset [75, 76]. In such a case, design of the metasurface for pure frequency mixing (serrodyne frequency translation) gives rise to a single spatiotemporal dynamic beam [76] while concurrent conversion of the frequency into different sidebands can lead to simultaneous generation of multiple dynamic beams periodically scanning the space at different rates [75].

In this paper, we will theoretically demonstrate generation of time-varying optical vortices based on TMMs with azimuthal frequency gradient. The topological charge of such a dynamic twisted light beam changes continuously and periodically in time with a linear dependence on time and azimuthal frequency offset in the TMM. The temporal variations in OAM yields a self-torqued the light beam which results to continuous angular acceleration of the light beam. These time-dependent features are characterized by a vortex with expanding and shrinking radius in time as schematically shown in Figure 1. We will mathematically establish the generation of such a vortex beam within a general theoretical framework and obtain a closed-form relation for its time-dependent topological charge. To numerically authenticate the concept, we will consider a reflective metasurface consisting of silicon nanodisk heterostructures integrated with indium-tin-oxide and gate dielectric layers on top of a metal-backed silicon slab which renders an electrically tunable guided mode resonance mirror. By dividing the metasurface into several azimuthal section wherein the nanodisk heterostructures are interconnected via nanobars acting as biasing lines and applying RF biasing signals with different frequencies into each section, a TMM with angular frequency gradient is realized. The direct dynamic photonic transitions of leaky-guided modes to different temporal frequencies lead to a frequency gradient in the optical field which subsequently gives rise to a dynamic time-varying optical vortex by virtue of coherent space-time path in the interference pattern. We will explore the role of modulation waveform and frequency gradient on the temporal evolution of twisted light beams which clearly illustrate the robust electrical tunability over the number of dynamic vortices and the degree of self-torque offered by the TMM.

The rest of this manuscript is organized as follows. In section 2, we will lay out the theoretical development of the

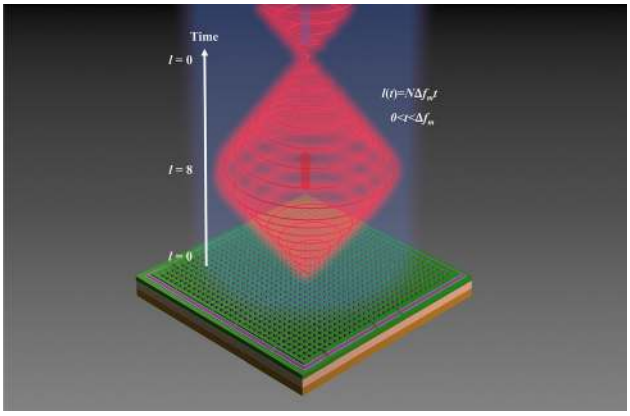


**Figure 1:** The schematic demonstration of a time-varying optical vortex generated by reflection of laser beam from a time modulated metasurface with an azimuthal frequency gradient. The beam is characterized by a ring-shaped intensity pattern whose radius increases and decreases continuously and periodically in time due to the variations in the topological charge.

concept. Section 3 discusses the design and numerical implementation of frequency gradient TMM. The simulation results are given in section 4. Finally, the conclusions are drawn in section 5.

## 2 Theoretical formulation

In this section, we aim at establishing the concept through a simplified theoretical formulation. Temporal modulation of metasurfaces will cause transition of the fundamental frequency (i.e., $f_0$) to the higher-order frequency harmonics (i.e., $f_p$) given by $f_p = f_0 + pf_m$, wherein the integer $p \in \mathbb{Z}$ indicates the order of generated frequency harmonic. Therefore, in contrary to static or quasi-static tunable metasurfaces, which are capable of controlling only the spatial characteristics of the scattered light beams, TMMs are able to manipulate the spectral content of the scattered fields as well.

Here, we consider a reflective TMM which is modulated via a modulation frequency that depends on the azimuthal angle (i.e., $f_m(\varphi)$) under illumination of a normally incident Gaussian beam at the frequency of $f_0$ propagating along $\hat{z}$ direction. The reflected field from the metasurface possesses a periodic temporal dependency that can be expressed as a summation over higher-order frequency harmonics via Fourier decomposition. Therefore, the incident and reflected waves can be expressed as

$$E_i(r, t) = E_0 \exp\left(-\frac{r^2}{w^2}\right)\exp(i\omega_0 t)\exp\left(i\frac{\omega_0}{c}z\right)$$

$$E_r(r, \varphi, t) = E_0 \sum_p e_p(r)\exp\left(i(\omega_0 + p\omega_m(\varphi))t\right) \exp\left(i\frac{\omega_0 + p\omega_m(\varphi)}{c}z\right) \quad (1)$$

where $\omega_0 = 2\pi f_0$ and $\omega_m = 2\pi f_m$ are the optical and modulation angular frequencies, respectively, $r$ and $\varphi$ denote the radial and azimuthal directions, respectively, $w$ is the Gaussian radius at the waist, $e_p(r)$ is the coefficient describing the radial dependency of the scattered field at the $p$th frequency harmonic, $c$ is the speed of light, and $E_0$ is the amplitude of the incident field. We consider an azimuthally linear gradient in the modulation frequency. For this purpose, the metasurface can be divided into $N$ equal azimuthal sections separated by angular intervals of $\Delta\varphi = 2\pi/N$ which yields a discrete angle-dependent modulation frequency of

$$f_m(\varphi) = f_{m,0} + \lfloor N\varphi/2\pi \rfloor \Delta f \quad (2)$$

where $f_{m,0}$ is a constant, $\Delta f$ is the azimuthal offset in the modulation frequency, and $\lfloor . \rfloor$ stands for the floor function. This expression takes into account the discretization of modulation frequency in a metasurface azimuthally divided into $N$ discrete sections such that the difference in the modulation frequency of adjacent sections can be obtained as $\Delta f_m = \lfloor N\Delta\varphi/2\pi \rfloor \Delta f = \Delta f$. Such a discretized modulation frequency profile allows for defining the overall temporal periodicity of scattered field from such a frequency gradient TMM as $T = 1/\Delta f$ [76, 79]. Plugging Equation (2) into Equation (1), the total reflected field in one cycle of such temporal modulation ($|t| \le 1/2\Delta f$) can be expressed as

$$E_r(r, \varphi, t) = E_0 \sum_p e_p(r)\exp\left(i\left(t + \frac{z}{c}\right)(\omega_0 + 2\pi f_{m,0})\right) \times \exp\left(i2\pi\left(t + \frac{z}{c}\right)p\Delta f\left[\frac{N\varphi}{2\pi}\right]\right) \quad (3)$$

Considering the spatial continuity of the scattered fields wavefront, the spatiotemporal azimuthal dependency of the reflected field can be simplified as $\exp\left(i\left(t + \frac{z}{c}\right)p\Delta f N\varphi\right)$ by setting aside the discretization errors. On the other hand, the ideal profile of a Bessel beam with the OAM state of $|l\rangle$ can be expressed as

$$E_l(r, \varphi, t) = A_0 \exp(-r^2/w^2) J_l(k_r r)\exp\left(i\left(t + \frac{z}{c}\right)\omega_0\right)\exp(il\varphi) \quad (4)$$

wherein $J_l(.)$ is the $l$-th order Bessel function, $A_0$ is a complex constant and $k_r = 2\pi/r_0$ is the radial wave number

determined by the radius of the Bessel beam ($r_0$). Comparing Equation (4) with Equation (3), it can be inferred that each frequency harmonic order $p$ in the reflected beam from the TMM with an azimuthally linear frequency gradient can be viewed as a dynamic optical vortex whose topological charge has a spatiotemporal dependency given by

$$l_p(t, z) = p\Delta f N\left(t + \frac{z}{c}\right) \tag{5}$$

This expression is valid in range of $|t| \le 1/2\Delta f$ corresponding to one cycle of modulation in the frequency gradient TMM and the topological charge will have a periodic behavior which repeats over time intervals of $T = 1/\Delta f$. As such, the time-varying topological charge resulting from *pth* order frequency harmonics is bounded within $-pN/2 \le l_p(t, z) \le pN/2$. It should be remarked that the outlined derivation here relies on the assumption of a discrete azimuthal frequency gradient profile to be able to define the temporal periodicity of the scattered field from the array as a function of azimuthal frequency offset. We note that a continuous change in the frequency is nonphysical and yields $N \to \infty$ and $\Delta f \to 0$ making the temporal periodicity of the frequency gradient array and the bounds of time-varying topological charges ill-defined.

For optical TMMs, the accessible modulation frequencies are a small fraction of the optical frequency $f_m \ll f_0$ due to the inherent speed of modulation mechanisms and the operation is typically limited to the adiabatic regime where the imparted energy to the system through modulation only manifests itself in frequency conversion. The significant difference between the scales of modulation and optical frequencies in such TMMS yields $\frac{\Delta f \lambda}{c} \ll 1$ leading to the weak spatial dependence of topological charge in dynamic vortices, i.e., the beam has to propagate over a distance of $10^3$–$10^5$ times the wavelength to experience a change in the topological charge. We note that while in general the optical vortices generated by frequency gradient TMMs are varying spatiotemporally, given the weak spatial dependency of topological charge in the adiabatic modulation regime and the scope of the work which is focused on time-varying topological charge, we have neglected the spatial term in Equation (5) to safely approximate the topological charge as $l_p(t) = p\,\Delta f\,N\,t$ in the nearfield regime. The time-varying topological charge in the generated optical vortices by the frequency gradient TMM leads to a time-varying OAM (per photon) of $\mathbf{L}_p(t) = \hbar p\,\Delta f\,N\,t$ whose derivative with respect to time yields a constant torque of $\tau = \hbar p\,\Delta f N$ acting on the light beam as it propagates in free-space. This self-torque is an intrinsic property of the generated light beams [31] due to the coherent space-time path in a beam with azimuthal frequency gradient. It should be emphasized that the time-varying OAM of $\mathbf{L}_p(t)$ corresponds to the time-domain vortex generated due to $p$th frequency harmonics and does not quantify the OAM of total time-domain scattered field from frequency gradient TMM which is a superposition of different vortices generated by distinct frequency harmonic orders. The OAM of the generated vortex beams due to $p$th frequency harmonic order is also evaluated more rigorously based on the canonical momentum method and its mathematical derivation is given in section S1 of the Supplementary Material which yields the same expression of $\mathbf{L}_p(t) = \hbar p\,\Delta f\,N\,t$.

The temporal variations in the OAM also lead to angular acceleration of the light fields corresponding to the time-varying optical vortices which can be obtained by the second-derivative of azimuthal position ($\varphi$) with respect to time in the phase front of reflected light at a fixed distance above the metasurface ($l_p(t, z)\varphi + \omega_0 t = \text{const}$). Unlike the light field of a static optical vortex which has a constant angular velocity of $\Omega = d\varphi/dt = -\omega_0/l$ and a zero acceleration, the light field of the time-varying vortices possess a time-dependent angular velocity of $\Omega(t) = d\varphi/dt = -\omega_0/[p\Delta f N(t + z/c)]$ and angular acceleration of $\alpha(t) = d^2\varphi/dt^2 = p\Delta f N\omega_0/[p\Delta f N(t + z/c)]^2$. As it can be seen, the sign of angular acceleration can be controlled by the sign of frequency offset along azimuthal direction ($\Delta f$).

As it has been recently shown in several works, engineering the modulation waveform of a TMM allows for controlling the spectral diversity of frequency harmonics in the output spectrum [62, 73, 76, 80, 81]. This enables control over the number of dynamic optical vortices in the reflected field from the TMM. For example, engineering the modulation waveform for serrodyne frequency translation to $f_0 + f_m$ yields a single dynamic beam whose time-varying topological charge is given as $l_1(t) = \Delta f\,N\,t$. Moreover, control over the azimuthal frequency gradient profile given in Equation (2) not only allows for adjusting the rate of temporal variations in the topological charge by tuning $\Delta f$ but also enables tuning the upper/lower bounds of topological charge in each cycle by control over the azimuthal division ($N$).

In order to gain a more intuitive insight into the operating principle of frequency gradient TMM, we consider a reflective TMM aperture divided into four azimuthal sub-apertures biased with modulation frequencies of $f_m = n\Delta f$ with $1 \le n \le 4$ denoting the index of the sub-apertures as shown in Figure 2a. Assuming that the metasurface is designed for pure frequency mixing (i.e., serrodyne frequency translation into $f_0 + f_m$), the reflected wavefront from each sub-aperture is shown as a plane wave

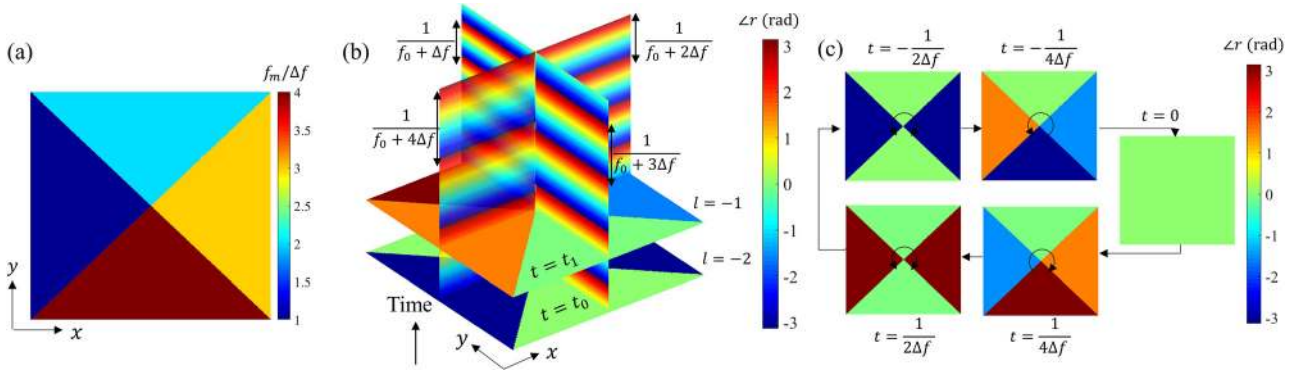


**Figure 2:** **(a)** Aperture of a TMM azimuthally divided into four equal sub-apertures with a modulation frequency offset of $\Delta f$. **(b)** The wavefront of reflected fields from the sub-aperture depicted as plane waves propagating in time. The transverse planes show the variation of azimuthal phase profile across the aperture as a function of time. (c) The azimuthal phase profile of the reflected light across the aperture at different instants of time.

propagating in time in Figure 2b in the time interval of $|t| < 1/2\Delta f$. Looking at the transverse phase profile of reflected light across the aperture at different instants of time illustrates an azimuthal phase gradient which corresponds to the helical wavefront of an optical vortex. In particular, the azimuthal coherent path of light in the resultant interference pattern is a function of time due to the azimuthal frequency offsets applied to the sub-apertures which yields a change in the azimuthal phase variations. Figure 2c demonstrates the phase profile of the reflected light at the time instants of $t = l/4\Delta f$ with $l$ being an integer ranging from −2 to +2. The results clearly show generation of an azimuthal phase gradient of $l\varphi$ at each instant of time which subsequently leads to generation of optical vortices with a time-varying topological charge circumscribed within the range of $-2 \le l(t) \le +2$.

## 3 Metasurface design

To numerically authenticate the idea of time-varying optical vortex generation based on TMMs and verify the validity of the theoretical discussions in previous section, we will design and model a reflective TMM by configuring a guided mode resonance mirror (GMRM) structure [82] as a dual-gated field effect modulator whose geometry is depicted in Figure 3a. For this purpose, we employ indium-tin-oxide (ITO) as an electro-optical material and utilize $Al_2O_3/HfO_2$ nanolaminates (HAOL) [83, 84] as the gate dielectrics. The metasurface is consisted of a periodic array of sub-wavelength Si/HAOL/ITO/HAOL nanodisk heterostructures located on top of a silicon guiding core, followed by a silica optical buffer and a gold back mirror. The metasurface is azimuthally divided into 16 sections wherein nanodisk heterostructures are interconnected with nanobar heterostructures serving as biasing lines while adjacent azimuthal sections are isolated from one another by termination of the biasing lines. The angular sectioning of the metasurface can be seen more clearly in the top-view shown in Figure 3b where the boundaries between the sections are marked by the dashed lines. The proposed configuration allows for addressing each azimuthal section independently from the side with two sets of voltages addressing the top doped silicon layer, ITO layer and bottom silicon layer via contact electrodes, as illustrated in Figure 3a. The dual-gated biasing leads to field effect modulation of carrier concentration within the ITO layer and as a result two charge accumulation/depletion layers will be formed at the interface of ITO with top and bottom HAOL gate dielectrics [83]. The voltage-controlled tunability of carrier concentration in these active regions enables a real-time control over the light–matter interaction at nanoscale which can yield a wide dynamic phase modulation via a proper photonic design of the building blocks. In principle, the high drift velocity of electrons in a field effect modulator allows for attaining modulation frequencies up to several THz [85]. Nevertheless, the modulation speed of electro-optical platforms is ultimately limited by the speed of interconnects and the capacitive delay of the elements, bringing down the accessible modulation frequencies to several GHz [86]. Employing RF biasing signals of different frequencies for modulation of different azimuthal sections of the metasurface renders a TMM with an azimuthal frequency gradient while offering a robust electrical tunability.

There have been several recent experimental realizations of ITO-integrated metasurfaces offering voltage-controlled real-time tunability of the optical response [83, 87–89]. The proposed unit-cell can be implemented by

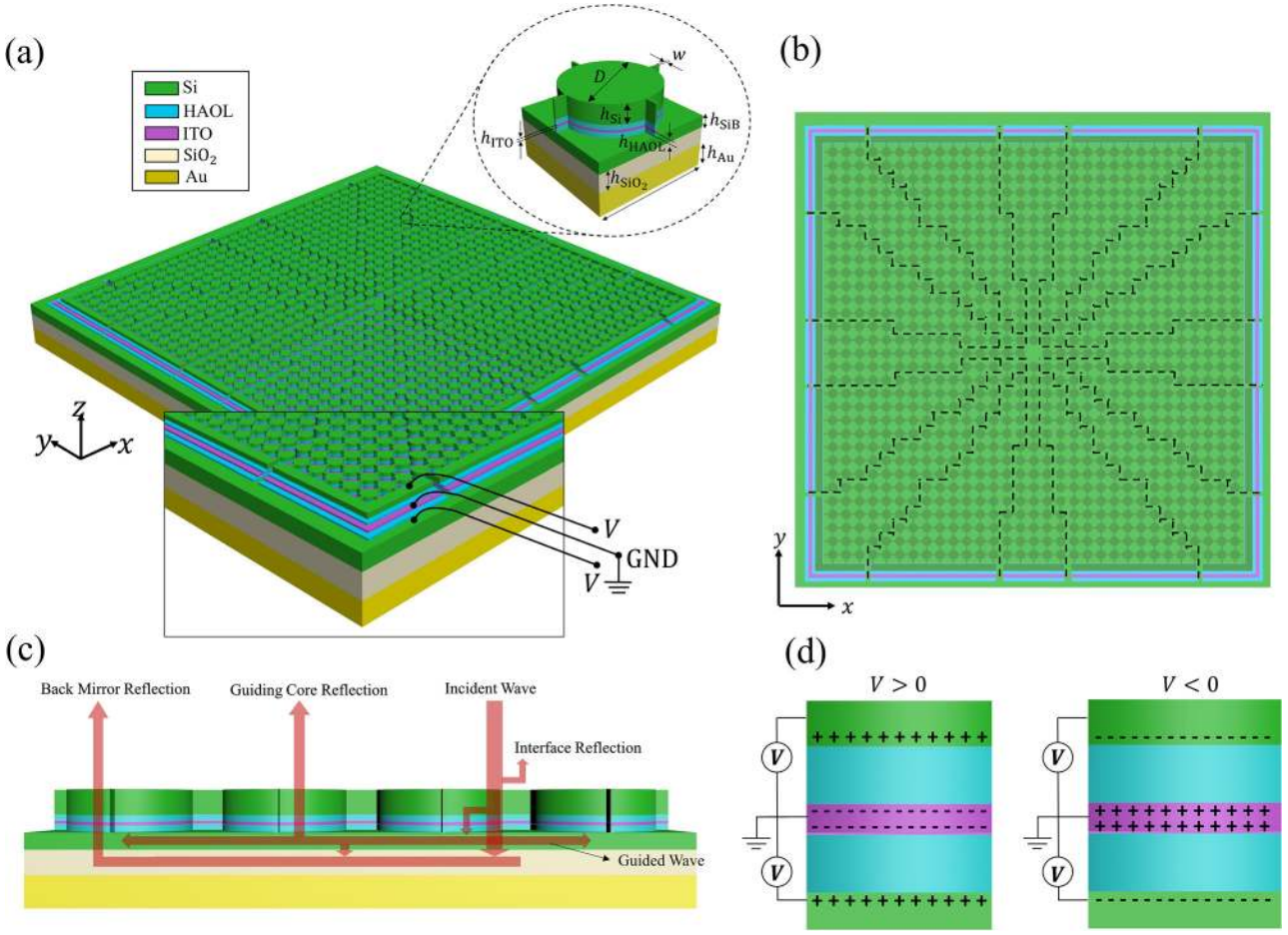


**Figure 3:** **(a)** The schematic depiction of the proposed metasurface consisting of an array of subwavelength Si/HAOL/ITO/HAOL nanodisk heterostructures placed on top of a silicon guiding core followed by a silica buffer and a gold back mirror rendering a field-effect tunable GMRM. The metasurface is azimuthally divided into 16 equal sections wherein nanodisks are interconnected via nanobar heterostructures serving as biasing lines, while adjacent sections are isolated via termination in the biasing lines. The geometrical parameters of the unit cell shown in the zoomed-in view are chosen as $D = 581$ nm, $h_{Si} = 362$ nm, $h_{HAOL} = 28$ nm, $h_{ITO} = 9$ nm, $h_{SiB} = 171$ nm, $h_{OB} = 450$ nm, $w = 10$ nm and $\Lambda = 613$ nm. The metasurface is under illumination of a normally incident TE polarized wave. **(b)** The top-view of the metasurface where the boundaries between the azimuthal sections are denoted by the dashed lines. **(c)** Demonstration of the wave coupling and light interaction mechanisms in the GMRM. Multiple optical paths in reflection and particularly the elongated path through in-plane propagation of guided waves yield enhanced tunability of the optical response through enhanced light–matter interaction with the active regions formed within ITO layer under applied bias voltage. **(d)** Formation of charge accumulation/depletion layers at the top and bottom interfaces of ITO-HAOL and Si-HAOL under field effect in the dual-gate biasing scheme.

using standard electron beam lithography (EBL) and multiple deposition steps. To this aim, the Au back mirror can be deposited on a quartz glass substrate with the aid of thermal evaporation. Then, the guiding core, which is made of Si, can be subsequently sputtered and boron dopants can be applied for achieving the desired background carrier concentration. Afterwards, the HAOL gate dielectric can be grown on top of the Si guiding core using the atomic layer deposition (ALD) process [83]. As the next step, the ITO layer can be sputtered on the bottom gate dielectric by using RF magnetron sputtering in an oxygen/argon plasma where the flow rate of argon/oxygen gas can be controlled to achieve different background carrier concentrations in the ITO layer. Subsequently, the top gate dielectric can also be grown on the ITO layer by using the ALD process. The top Si layer can be then sputtered on the top gate dielectric layer, followed by doping through boron dopants [87]. Finally, to attain the desired geometry shape, the stack of Si, ITO and HAOL layers should be patterned using EBL system by developing a photoresist film to define the pattern. The photoresist eventually must be removed via lift-off in acetone.

It should be mentioned that we have recently employed a similar azimuthal division approach for achieving hybrid

mode-frequency division multiple access via topological space-time photonic transitions in angular-momentum-biased metasurfaces [74]. While the underlying concept in the previous work has been based on imprinting an azimuthal modulation phase delay across the metasurface, the current work relies on an azimuthal frequency gradient. Moreover, the modulation mechanism of the time-modulated metasurface considered in this work is based on tuning a GMRM in an ITO-integratedsemiconductor-insulator-semiconductors unit cell which yields a higher efficiency and uniformity of amplitude compared to modulation based on tuning of the magnetic dipole resonance supported by the metal-insulator-semiconductor unit cell utilized in the previous work.

## 3.1 Unit-cell design

ITO is a degenerately doped semiconductor which has been commonly used in high-speed electro-optical modulators via integration into waveguide geometries [86]. The degenerate doping level of ITO (ranging from $10^{19}$ $cm^{-3}$ to $10^{21}$ $cm^{-3}$) brings its plasma frequency to the infrared optical frequency regime. This can lead to formation of epsilon-near-zero (ENZ) regions under applied bias voltage yielding a significant enhancement of light–matter interaction which can be leveraged for obtaining a widely tunable optical response. ITO has been recently integrated into several geometrically-fixed resonant metasurfaces with different motifs in order to obtain a dynamic phase modulation in reflection and/or transmission modes [83, 84, 88–93]. Due to the small volume of active regions formed upon charge accumulation/depletion, limited tunability of carrier concentration prior to the breakdown of gate dielectrics and the high material loss of ITO, these metasurfaces operate near critical coupling regime associated with maximal absorption to achieve a wide phase swing through modulation of absorption and transition of the resonance between over-coupled and under-coupled states [89]. This approach typically yields a limited dynamic phase span (less than $2\pi$) with a dramatic variation in the amplitude during phase modulation. Multigate biasing has been recently proposed to increase the dynamic phase span of ITO-integrated metasurface by increasing the volume of active regions in the ITO layer [83]. HAOL has also been proposed as a gate dielectric with optimal trade-off between DC permittivity and breakdown field which can maximize the accumulation of carrier concentration under applied bias voltage, further increasing the span of phase modulation [83]. Moreover, exploiting high quality-factor guided mode resonances (GMRs) in an ITO-integrated GMRM has proved to be effective for mitigating the nonuniformity of amplitude across the phase modulation range [84]. This is attributed to the elongated lifetime of photons and enhancement of field confinement within the ITO-integrated resonators in GMRM [82, 94] which yield a steep reflection phase spectrum and lead to a larger tunability in the resonant response, thus allowing for operation further from the critical coupling point.

Here, we employ a GMRM configured as a dual-gated field effect modulator for dynamic phase modulation in the reflection mode. The aim is to maximize the dynamic phase span of the reflected light from the metasurface under illumination of a normally incident transverse electric (TE)-polarized plane wave while maintaining minimal variations in the reflection amplitude. For this purpose, the structural parameters of the building blocks are judiciously chosen to support an over-coupled GMR with a moderately high quality-factor in the absence of applied bias voltage. The field effect modulation of carrier concentration in the ITO layer integrated into the GMRM can drive the resonance into the under-coupled state with an enhanced tunability by virtue of elongated photon lifetime and field confinement within the resonant structure. In order to gain more insight into the physics of GMRM [82, 94], the coupling and radiation mechanisms in the structure are schematically depicted in Figure 3c. When an incident beam impinges on the structure, it is partially reflected back from the first interface formed by silicon nanodisks (interface reflection). Another optical path in the reflection is consisted of multiple reflection of light between the optical buffer and the back-mirror passing through the layered structure (back-mirror reflection). The rest of incident power will be coupled into two counter-propagating guided waves supported in the silicon guiding core and silicon grating which leaks into free-space gradually while propagating in plane (guiding core reflection). This clearly illustrates the enhanced tunability of optical response a result of multiple optical paths in reflection and particularly the in-plane propagation of guided waves.

The structural parameters of the unit cell shown in Figure 3a are fixed as $\Lambda = 613$ nm, $h_{ITO} = 9$ nm, $h_{Si} = 362$ nm, $h_{HAOL} = 28$ nm, $h_{SiB} = 171$ nm, $D = 581$ nm and $h_{OB} = 450$ nm based on a careful and comprehensive parametric study. Both silicon and ITO layers are considered to be n-type doped with the background carrier concentrations of $N_{Si} = 1 \times 10^{19}\,cm^{-3}$ and $N_{ITO} = 3 \times 10^{20}\,cm^{-3}$, respectively. The optical response of the metasurface is calculated by utilizing rigorous coupled wave analysis (RCWA). In the optical simulations, the permittivity of HAOL is considered as $\varepsilon_{HAOL} = 4.29$ and the dispersive

permittivity of gold substrate is expressed by the Drude model as $\varepsilon_{\mathrm{Au}}(\omega) = \varepsilon_\infty - \omega_p^2/(\omega^2 + i\Gamma\omega)$ in which $\varepsilon_\infty = 1.53$, $\Gamma = 2\pi \times 17.64$ THz and $\omega_p = 2\pi \times 2.069$ PHz. The dielectric permittivity of the ITO layer is also described by a Drude model in which $\varepsilon_\infty = 3.9$ and $\Gamma = 180$ THz. However, the plasma frequency (i.e., $\omega_p$) of the ITO is related to the electron carrier concentration (i.e., $N_{\mathrm{ITO}}$) as $\omega_p = \sqrt{N_{\mathrm{ITO}} e^2/\varepsilon_0 m^*}$ wherein $e$ is the electron charge, $\varepsilon_0$ is vacuum permittivity, and $m^* = 0.35 m_0$ is the electron effective mass with $m_0 = 9.1 \times 10^{-31}$ kg being the electron rest mass [82]. The carrier-induced changes in the permittivity of silicon layers are also taken into account by utilizing Plasma-Drude model which expresses the permittivity of silicon as $\varepsilon_{\mathrm{doped-Si}}(\omega) = \varepsilon_{\mathrm{undoped-Si}}(\omega) - \frac{e^2}{\varepsilon_0 \omega}\left(\frac{N}{m_N^* \omega + ie/\mu_N} + \frac{P}{m_P^* \omega + ie/\mu_P}\right)$, wherein $N(P)$ is the electron (hole) density, $\mu_N(\mu_P)$ is electron (hole) mobility, and $m_N^*(m_P^*)$ is electron (hole) conductivity effective mass. In this work, each of the mentioned parameters are selected to be $\mu_N = 80\ \mathrm{cm^2V^{-1}S^{-1}}$, $\mu_P = 60\ \mathrm{cm^2V^{-1}S^{-1}}$, $m_N^* = 0.27\, m_0$ and $m_P^* = 0.39\, m_0$ [86]. The electro-optical response of the metasurface is rigorously characterized by linking the carrier dynamics in ITO and Si layers to the optical response via carrier-dependent dispersion models while accurately taking into account the inhomogeneous profile of permittivity within active regions through a fine multilayer discretization. The simulation of carrier dynamics is carried out using Lumerical Device software which self consistently solves the Poisson and drift-diffusion equations via finite-element method while using Fermi–Dirac statistics for drift-diffusion.

Under the application of two sets of negative bias voltages between the lower/upper doped Si and ITO layer, free electrons will be depleted at the top and bottom ITO-HAOL interfaces that leads an increment in the real part of ITO permittivity and a decrement in its imaginary part. Meanwhile, electrons will be accumulated at the interfaces of Si-HAOL to satisfy the charge conservation as shown schematically in Figure 3d. On the other hand, when the applied bias voltages are positive, free electrons will be accumulated at the top and bottom ITO-HAOL interfaces as depicted in Figure 3d which will result into the decrement in the real part of ITO permittivity while simultaneously increasing its loss (i.e., imaginary part of ITO permittivity will be increased). By further increasing the applied bias voltage, real part of ITO permittivity continues to decrease until it eventually crosses the ENZ region where $-1 < \mathrm{Re}\{\varepsilon_{\mathrm{ITO}}\} < +1$, which subsequently results in the change of active layers from dielectric to plasmonic. It should be noted that under positive applied bias voltages, electrons will be depleted at the Si-HAOL interfaces before the length of the depletion layer reaches its maximal value at a certain positive threshold voltage ($V_T$). When the applied bias voltage exceeds this threshold voltage, Si will be inverted from n-type to p-type at Si-HAOL interfaces which gives rise to accumulation of hole carriers in these regions by increasing the applied bias voltage. While the tunable optical response of the metasurface predominantly relies on the charge accumulation/depletion at ITO-HAOL interfaces, the carrier-induced changes in the permittivity of Si at Si-HAOL interface are also accurately taken into account in our modelling. Further details regarding device simulation and electro-optical modelling are provided in section S2 of Supplementary Material.

The amplitude and phase of the reflection from the dual-gatedITO-integrated GMRM are calculated and plotted in Figure 4a,b, respectively as functions of incident wavelength for different applied bias voltages. As it can be seen from the results, the metasurface supports a resonant mode at no-bias which can be identified by the dip in the reflection amplitude spectrum and the spectral phase accumulation of $\approx 2\pi$. The nearfield distributions of magnetic and electric fields within the unit cell heterostructure are demonstrated in Figure 4c,d, respectively at the resonant wavelength of $\lambda = 1.552$ μm at no-bias in the $x - z$ plane. The magnetic field shows an in-plane standing wave pattern corresponding to the interference between counter-propagating guided waves which is a manifestation of GMR. This is while the electric field is strongly localized at the HAOL/ITO/HAOL stack which enables substantial tunability of light–matter interaction at nanoscale by formation of charge accumulation/depletion layers at the top and bottom ITO-HAOL interfaces under applied bias voltage.

Increasing the applied bias voltage from $V = -10$ V to $V = 5$ V, the resonance blueshifts toward shorter wavelengths as a result of decrement in the real part of permittivity of active regions within the ITO layer with a simultaneous decrement in the amplitude of resonant dip due to increased carrier-induced loss as can be observed in Figure 4a,b. The resonance is at the over-coupled state for applied bias voltages below $V = 5$ V which can be observed from the wide spectral phase agility. At $V = 5$ V, a near-unity absorption is attained at the resonance with a slip in the phase spectrum which corresponds to the critically-coupled resonant state due to the formation of ENZ regions at the top and bottom ITO-HAOL interfaces. Increasing the bias voltage beyond 5 V, the resonance undergoes transition from over-coupled to under-coupled state as identified by the flip in the phase spectrum. At the same time, the direction of the spectral shift of the resonance is reversed as a result of

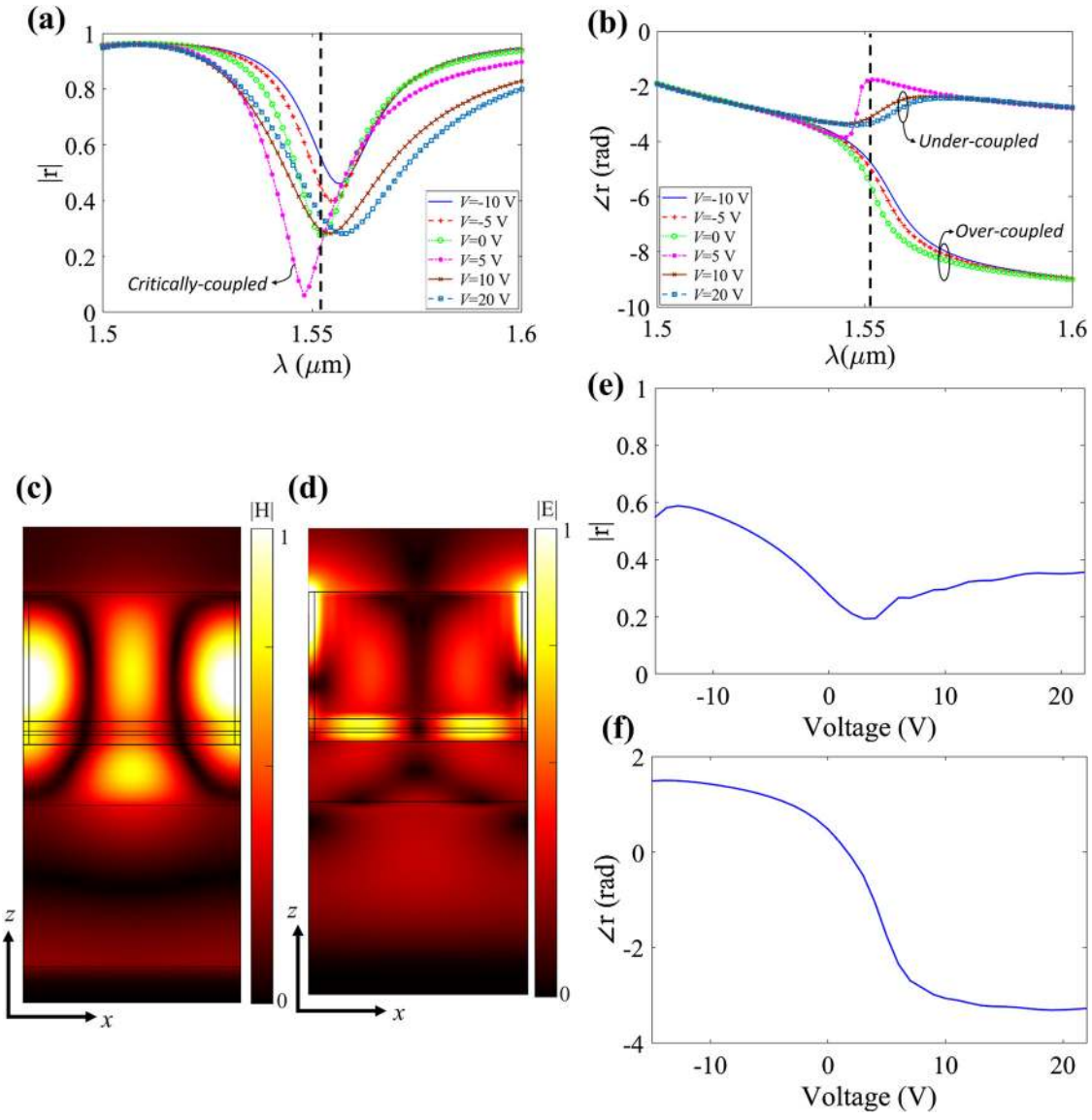


**Figure 4:** **(a)** The amplitude and **(b)** phase of reflection calculated as functions of wavelength at different applied bias voltages. The vertical dashed line marks the operating wavelength of $\lambda_0 = 1.552\,\mu m$ yielding maximal dynamic phase span with minimal variations in the amplitude. The calculated nearfield distribution of **(c)** magnetic and **(d)** electric field within the unit cell in the x-z plane. The **(e)** amplitude and **(g)** phase of reflection calculated as functions of applied bias voltage at the operating wavelength of $\lambda_0 = 1.552\,\mu m$.

change in the property of ITO active regions from dielectric to plasmonic which leads to shrinking of the effective thickness of dielectric regions in the HAOL/ITO/HAOL stack.

The transition of the resonance from over-coupled to under-coupled state and its simultaneous spectral shift under applied bias voltage yield a wide phase swing at the operating wavelength of $\lambda = 1.552\,\mu m$ which is denoted by the dashed line in Figure 4a,b while avoiding dramatic variations in the reflection amplitude. The calculated amplitude and phase of reflection at this wavelength are shown in Figure 4e,f as functions of applied bias voltage ranging from –15 to 22 V prior to reaching the breakdown field in the HAOL gate dielectric layers ($E = 7.2\,MV/cm$) [83]. A dynamic phase span of 270° is attained with reflection amplitude varying between 0.6 and 0.2.

## 3.2 Time-modulated response of the designed building-block

In this subsection, we will characterize the frequency conversion performance of the designed metasurface upon introducing temporal modulation. In a time-

modulated GMRM, the frequency conversion can be described as the direct dynamic photonic transitions of guided modes due to vertical frequency shifts in the dispersion band diagram [52]. The frequency conversion performance of a TMM is determined by the temporal evolution of the amplitude and phase at the steady-state, i.e., a desired spectral diversity of frequency harmonics in the output spectrum dictates the temporal variations of the fields. In the adiabatic regime of modulation ($f_m \ll f_0$), a one-to-one mapping can be made between the steady-state scattered fields from a TMM at each instant of time to the quasi-static fields corresponding to the applied bias at that time instant [62, 73, 76]. This allows for a control over the spectral diversity of frequency harmonics by adjusting the modulation waveform. Nevertheless, ideal realization of an output frequency spectrum requires an independent control over the temporal variations of amplitude and phase which proves to be prohibitively challenging in tunable optical metasurfaces. While phase-only temporal modulation can be adopted to arrive at a non-ideal output spectrum, utilizing an evolutionary algorithm for optimizing the modulation waveform can yield a more optimal response by taking into account the correlation and trade-offs between phase and amplitude. Following this approach, we express the modulation waveform of TMM in the form of a truncated Fourier series with eight terms as $V(t) = \sum_{n=1}^{8} a_n \cos(n\omega_m t) + b_n \sin(\omega_m t)$ while assuming a modulation frequency of $f_m = 10\,\text{GHz}$, and employ genetic algorithm (GA) to optimize its coefficients toward obtaining the desired spectral diversity of harmonics. The output spectrum is obtained by constructing the steady-state time-domain reflected field through mapping the response at each instant of time to the quasi-static response corresponding to the instantaneous bias voltage and subsequently taking the Fourier transform. Specifically, we have considered two cases of pure frequency mixing and concurrent dual-frequency generation. For this purpose, we have defined the objectives of the optimization to be maximized as the normalized conversion efficiency to the desired frequency harmonic which are given by the reflected power residing at the desired frequency harmonics over the total reflected power. The objective functions corresponding to the cases of pure frequency mixing and concurrent dual frequency conversion are expressed as $|r_{+1}|^2/\sum_i |r_i|^2$ and $(|r_{+1}|^2 + |r_{-1}|^2)/\sum_i |r_i|^2$, respectively, wherein $r_i$ denotes the reflection coefficient corresponding to the $i$th frequency harmonic. The optimized modulation waveforms and their corresponding normalized output spectrum frequencies are obtained and plotted in Figure 5.

Figure 5a shows the optimized waveform corresponding to the case of pure frequency mixing which exhibits a sawtooth-like pattern with broken time-reversal symmetry. This is consistent with the phase modulation prescription for serrodyne frequency translation which requires a sawtooth temporal phase profile modulating the quasistatic phase linearly over 2π span at each cycle of modulation ($\angle r(t) = \omega_m t$) [62, 76, 80, 81]. The output spectrum of the TMM corresponding to this case is shown in Figure 5b by plotting the normalized conversion efficiency of different frequency harmonics defined as $|r_{n,i}|^2 = |r_i|^2/\sum_i |r_i|^2$. As it can

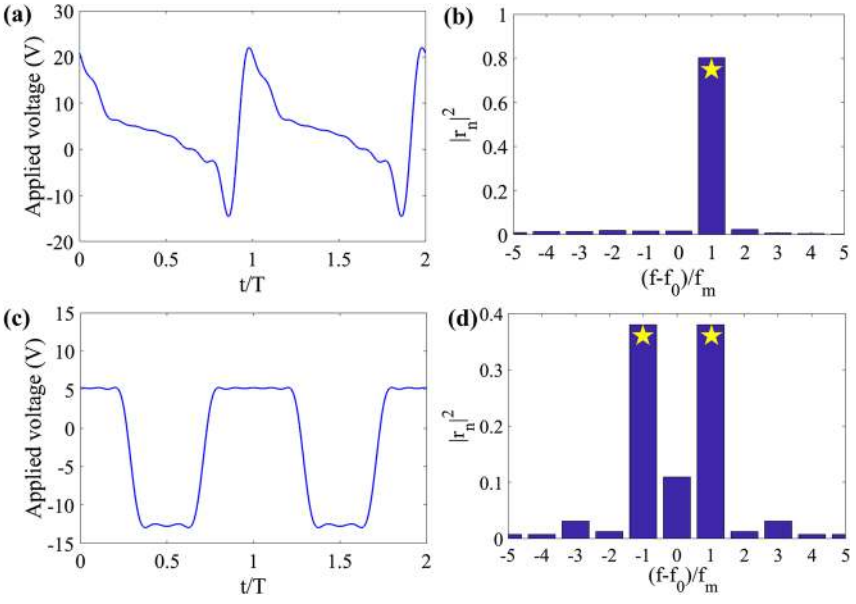


**Figure 5:** **(a)** The optimized modulation waveform and **(b)** the calculated normalized conversion efficiency of the TMM to different frequency harmonics, corresponding to the case of pure frequency mixing. **(c)** and **(d)** show the same for concurrent dual frequency generation. The desired mixing products are marked by star in the output spectra plotted in (c) and (d).

be seen, most of the power is residing at the first up-modulated frequency harmonic (i.e., $f_{+1} = f_0 + f_m$) marked by the star with a normalized frequency conversion efficiency of $|r_{+1}|^2/\sum_i |r_i|^2 = 81\%$. The non-unity conversion efficiency is attributed to the limited phase span and nonuniform amplitude of the quasi-static response. It should also be noted that despite the relatively high normalized frequency conversion efficiency, the overall frequency conversion efficiency is limited as the total reflected power is 8.88% due to the high dissipative loss in the metasurface metasurface operating near the critical coupling point.

Figure 5c demonstrates the modulation waveform corresponding to the case of concurrent dual frequency generation exhibiting a rectangle-like pattern with time-reversal symmetry. This waveform is in accordance to the required temporal phase modulation for conversion of the incident power to the first frequency sidebands given by a binary 0/π profile at each cycle of modulation ($\angle r(t) = \angle\cos(\omega_m t)$) [62, 76]. The output spectrum of TMM corresponding to this waveform is shown in Figure 5d by plotting the normalized conversion efficiency to the frequency harmonics, indicating most of the power residing at the up- and down- modulated frequency harmonics marked by the stars. The normalized frequency conversion efficiency to the first-order frequency harmonics is quantified as $(|r_{+1}|^2 + |r_{-1}|^2)/\sum_i |r_i|^2 = 76\%$. The imperfect suppression of fundamental frequency and other undesired mixing products in this case is due to the non-ideality in the temporal variations of amplitude which cannot provide a balanced modulation of loss and gain at each cycle of modulation required for conversion of the reflected power to the first sidebands with unitary efficiency [62, 76]. The total reflected power in this case is 17.42% in the account of dissipative loss which limits the overall frequency conversion efficiency of the ITO-integrated metasurface.

# 4 Generation of time-varying optical vortices

In this section, we will theoretically demonstrate generation of time-varying optical vortices and verify the predictions of simplified analysis in section 2 for the temporal profile of topological charge, through simulation of an azimuthally divided finite metasurface based on the unit cell design in section 3. For this purpose, we will employ the optimized waveforms for pure frequency mixing and concurrent dual frequency generation in order to temporally modulate the metasurface while incorporating a progressive offset in the modulation frequency of azimuthal sections to render a TMM with azimuthal frequency gradient. A metasurface consisting of $31 \times 31$ unit cells is considered which is divided into $N = 16$ azimuthal sections as described in the previous section. Due to the expensive computational cost associated with full-simulation of such large-area finite metasurface with multiscale features in space-time, we use adiabatic analysis in time while employing field equivalence principle based on the assumption of local periodicity in the response of azimuthal sections to obtain the steady-state optical response of the metasurface in space-time [73, 76]. For this purpose, we have calculated the steady-state time-domain local response of unit cells through one-to-one mapping of reflection amplitude and phase at each instant of time to their quasi-static counterparts obtained from full-wave periodic RCWA simulations, according to the applied modulation waveform and frequency to each azimuthal section. The obtained local fields are then used to calculate the equivalent time-domain electric and magnetic surface currents across the aperture of the metasurface at each instant of time in the steady-state. The time-domain scattered fields can be subsequently found anywhere in the space by adopting proper Dyadic Green's functions. It should be noted that imprinting a frequency gradient on the metasurface aperture requires independent addressing of each azimuthal section. As such, the biasing lines connecting the nanodisk heterostructures within each azimuthal section should be terminated at the edges of each section which affects the local phase modulation and frequency conversion of the metasurfaces in these regions. In the following analysis, we have dismissed such a local perturbation in the optical response by assuming that the voltage-dependency of the optical response does not vary across the metasurface aperture. The effect of termination of biasing lines on the performance of TMM is studied comprehensively in section S3 of Supplementary Material. It is shown that the adverse effects of such perturbation can be compensated by enlarging the metasurface aperture as it increases the number of interconnected unit cells. It is noteworthy that due to the topological robustness and self-healing property of optical vortices, the functionality of OAM-generating metasurfaces is robust against structural nonuniformities and local perturbations.

We consider an azimuthally linear frequency gradient as $f_m(\varphi) = 16(\varphi/2\pi)\Delta f$ imprinted on the time-modulated metasurface with $\Delta f = 1\,\text{GHz}$ that yields a time-interval of $T = 1$ ns for temporal variations in topological charge. This choice of frequency offset has been made to attain an ultrafast dynamic twisted beam with a maximal modulation

frequency of 16 GHz which can be realized by electro-optical modulation [86]. For this purpose, we assign a modulation frequency of $f_m = i\Delta f$ to each azimuthal section ($i = 1, 2, \ldots, 16$) of the metasurface as shown in Figure 6a. It should be emphasized that in the adiabatic regime of modulation ($f_m \ll f_0$), the spectral diversity of generated frequency harmonics by the TMM is independent from the modulation frequency, and $f_m$ merely determines the spectral position of harmonics. The metasurface is illuminated by a normally incident Gaussian beam with a waist radius of $w = 13\Lambda$. Employing the modulation waveforms corresponding to pure frequency mixing and concurrent dual-frequency generation while incorporating the azimuthal frequency gradient in biasing leads to generation of one and two dominant dynamic optical vortices in time-domain reflected field, respectively by virtue of the space-time coherent path in the interference pattern of the first-order frequency harmonics ($p = \pm 1$) whose temporal evolution are schematically depicted in Figure 6b,c, respectively. The spatiotemporal modulation waveforms in these cases can be expressed as $V(t) = \sum_{n=1}^{8} a_n \cos(2\pi n f_m(\varphi)t) + b_n \sin(2\pi n f_m(\varphi)t)$. According to the given formulation in section 2, the topological charge of these vortices changes periodically in the range of $-8 \le l_{\pm 1}(t) \le +8$ within time intervals of $T = 1/\Delta f = 1$ ns at the steady-state. It should be noted that such temporal variations in the topological charge can be characterized by measuring the azimuthal frequency gradient of the light beam. Rego et al. have reported experimental measurement of an ultraviolet time-varying OAM with a topological charge varying between 17 and 34 within 20 fs time interval generated via a nonlinear process, by exploiting a cylindrical mirror-flat-grating spectrometer to transform the azimuthal frequency chirp into a spatial chirp [31].

Figure 6d,e demonstrate the calculated real-part and intensity of the electric field reflected from the TMM biased with the sawtooth-type waveform optimized for pure frequency mixing while including the azimuthal frequency gradient, respectively across the transverse $x$-$y$ plane located at a distance of $2\lambda_0$ above the metasurface at different instants of time $t = l/16\Delta f$ within one cycle of periodic modulation of the frequency gradient system ($-1/2\Delta f \le t \le 1/2\Delta f$). The real-part of the fields clearly shows the time-varying twist in the wavefront of light associated with the phase winding number of an optical vortex with an OAM state of $|l_{+1}(t)\rangle = |16\Delta f t\rangle$ at the time instant of $t$. Moreover, the intensity profiles illustrate formation of an optical vortex with a dark central spot whose radius is varying in time. In particular, the radius of the vortex is maximal at $t = -1/2\Delta f$ associated with the OAM state approaching $|l_{+1}\rangle = |-8\rangle$ which shrinks by time-evolution prior to reaching zero at $t = 0$ associated with the OAM state of $|l_{+1}\rangle = |0\rangle$. Beyond this time instant, the radius of vortex starts to increase until reaching its maximal value again at $t = 1/2\Delta f$ corresponding to the OAM state approaching $|l_{+1}\rangle = |+8\rangle$. It can also be seen from the presented results that the field profiles at $t = -1/2\Delta f$ and $t = +1/2\Delta f$ are exactly the same due to periodicity of the temporal variations in the generated dynamic beam. The periodicity condition and continuity in the OAM states leads to generation of a superposition OAM state of $|+8\rangle + |-8\rangle$ at the time instants of $t = -1/2\Delta f$ and $t = +1/2\Delta f$. The temporal evolution of this dynamic optical vortex in 3D space can be seen more clearly in the Supplementary Movie 1. We note that the nearfield profile of time-domain reflected field is perturbed and lacks the mode purity compared to the ideal donut-shaped profile of an optical vortex which is attributed to the coexistence of several time-varying vortices in the time-domain field with different rates in temporal evolution of topological charge $l_p(t) = pN\Delta f t$ corresponding to the undesired frequency mixing products ($p \neq +1$). As discussed and shown in section 3.2, the normalized efficiency of pure frequency mixing to the up-modulated frequency harmonic ($p = +1$) in the designed unit cell is limited to 81% due to the limited dynamic phase span and nonuniform variations of amplitude across the phase modulation range. This means that 19% of the reflected power is residing at undesirable harmonics which perturb the nearfield profile of the time-domain reflected field compared to a single time-varying optical vortex. In order to further clarify the effect of imperfect frequency mixing in perturbation of the time-domain nearfield profiles, we have calculated the results for a case with near-unity frequency conversion efficiency afforded by the full dynamic phase span and uniform amplitude of the quasi-static response and the results are included in section S4 of the Supplementary Material which show a significant improvement in the nearfield profile of the generated time-domain field and its mode purity.

Next, we adopt the rectangle-like waveform optimized for concurrent dual frequency generation to bias the frequency gradient TMM. The theoretical formulation in section 2 predicts generation of two dominant dynamic beams due to coherent space-time path in the interference between up- and down-modulated harmonics such that the reflected light exhibits a dynamic superposition of state of $|l_{+1}(t)\rangle + |l_{-1}(t)\rangle = |-16\Delta f t\rangle + |16\Delta f t\rangle$. The results of calculated real part and intensity of the reflected light from the TMM in this case are shown in Figure 6f,g across the transverse $x$–$y$ plane at different instants of time given by

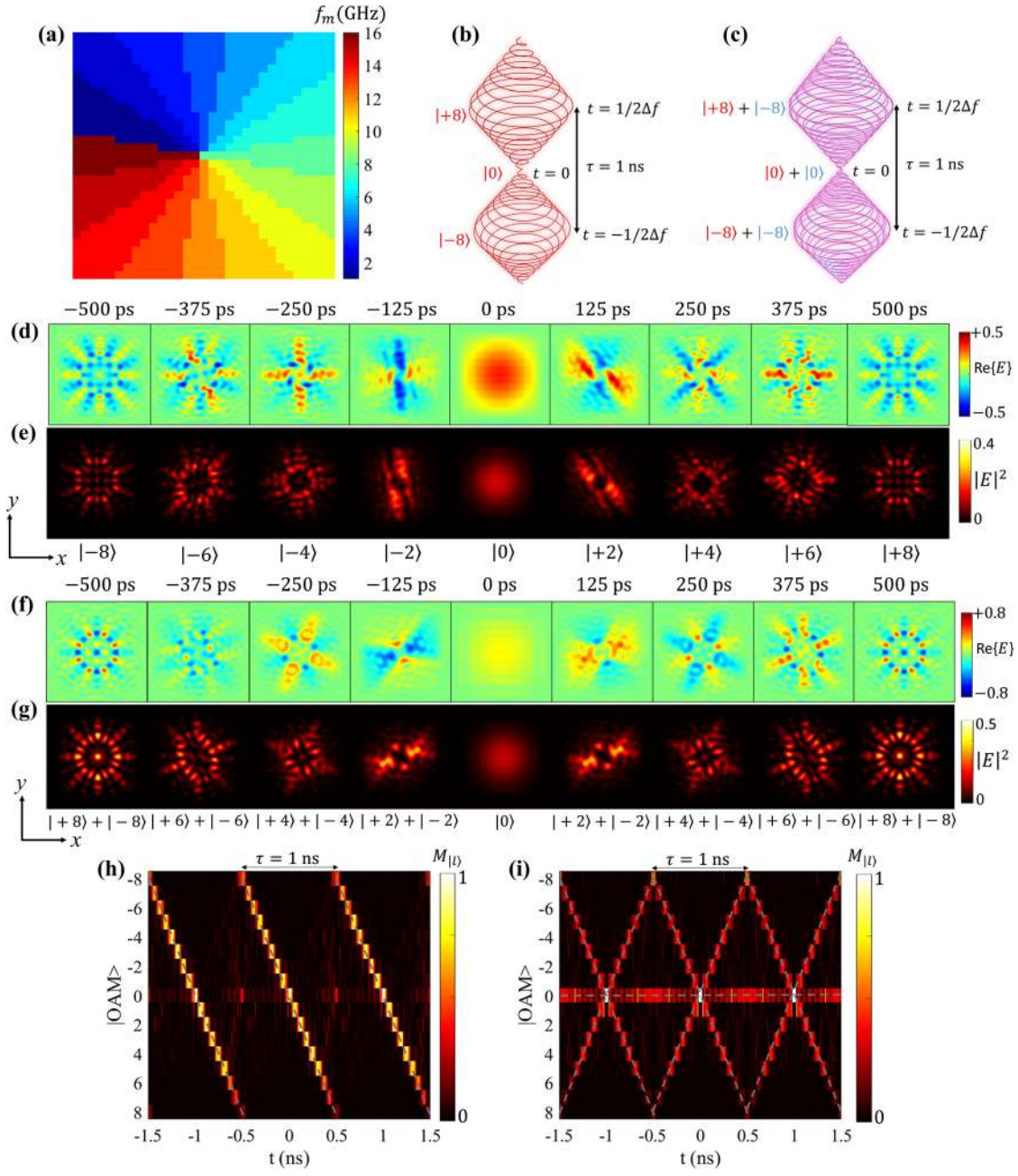


**Figure 6:** **(a)** The spatial distribution of modulation frequency across the metasurface aperture. The schematic illustration of the temporal evolution of dynamic optical vortices generated by frequency gradient TMM biased with **(b)** the sawtooth-like modulation waveform optimized for pure frequency mixing and **(c)** the rectangle-like waveform optimized for concurrent dual frequency generation. The calculated **(d)** real part and **(e)** intensity of the reflected electric field from the frequency gradient TMM biased with sawtooth-like waveform across the transverse x-y plane at a distance of $2\lambda_0$ above the metasurface at different instant of times within time-interval of $T = 1$ ns in the steady-state.**(f)** and **(g)** show the same as **(d)** and **(e)** for the frequency gradient TMM biased with the rectangle-like modulation waveform. The normalized spatial mode purity of the reflected light from the azimuthally divided frequency gradient TMM calculated as functions of OAM state and time for the cases of **(h)**sawtooth-like waveform and **(i)**rectangle-like modulation waveform.

$t = l/16\Delta f$ at one cycle of temporal periodicity. Similar to the previous case, the results abide well with the theoretical predictions showing an interference pattern of two dynamic optical vortices at each instant of time. The field profiles in this case exhibit a time-reversal symmetry due to symmetric modulation waveform with the intensity of the time-domain field at $t = l/16\Delta f$ being the same as that at $t = -l/16\Delta f$. The perturbation of time-domain field

compared to the dynamic interference pattern between two ideal time-varying optical vortices with the superposition state of $|l_{+1}(t)\rangle + |l_{-1}(t)\rangle = |-16\Delta f t\rangle + |16\Delta f t\rangle$ is a result of coexistence of other vortices in the time-domain field as a result of imperfect concurrent dual-frequency generation. The normalized frequency conversion efficiency in this case is limited to 76% indicating that 24% of the reflected power is residing at undesirable frequency mixing products leading to perturbation of the nearfield profile of the time-domain field. Supplementary Movie 2 shows the temporal evolution of this dynamic beam in 3D space.

In order to rigorously calculate the topological charge of the generated dynamic optical vortices as a function of time and clearly distinguish between the two cases with different modulation waveforms, we utilize the Fourier-Bessel decomposition in order to obtain the contribution of distinct orthogonal OAM states at each instant of time, as

$$e_l(t) = \frac{\int_0^{\infty}\int_0^{2\pi} d\varphi dr\, E(t, r, \varphi) E_l^*(r, \varphi, t)}{\int_0^{\infty}\int_0^{2\pi} d\varphi dr\, E_l^*(r, \varphi, t) E_l^*(r, \varphi, t)} \tag{6}$$

wherein $E(t, r, \varphi)$ is the reflected field profile at the time instant of $t$ and $E_l(t, r, \varphi)$ is the ideal profile of a Bessel beam given by Equation (4). Equation (6) is applied to the scattered time-domain fields obtained from simulation of the azimuthally discretized frequency gradient TMM ($E(t, r, \varphi)$) to obtain the spatial mode purity at each instant of time. We define the normalized spatial mode purity as $M_{|l\rangle}(t) = \left|e_{|l\rangle}(t)\right|^2 / \sum_{|l\rangle} \left|e_{|l\rangle}(t)\right|^2$ at each time instant which is calculated and plotted for reflected light beams from the frequency gradient TMM biased with the sawtooth-like and rectangle-like waveforms in Figure 6h,i, respectively.

As expected, in the case of pure frequency mixing the temporal variations in the spatial mode purity shown in Figure 6h indicates a dominant optical vortex whose OAM state of reflected light has a linear dependence on time as $|l_{+1}(t)\rangle = |16\Delta f t\rangle$ varying between $-8 \le l_{\pm 1}(t) \le +8$ within the time intervals of $T = 1/\Delta f = 1$ ns. We note that the normalized spatial mode purity obtained in this case is asymmetric with respect to $t = 0$ within the time interval of $|t| < 0.5$ ns due to broken time-reversal symmetry in the sawtooth-like modulation waveform. Moreover, the mode purities are also asymmetric with respect to $|l\rangle = 0$ due to absence of azimuthal symmetry in the frequency gradient TMM (modulation frequency increases by increment in the azimuthal angle). Specifically, the normalized spatial mode purity in this case increases from 46.12% at the state of $|l_{+1}(-500^{\text{ps}})\rangle = -8$ to 99.94% at the $|l_{+1}(0^{\text{ps}})\rangle = 0$ and then decreases to 16.84% for the topological charge of $|l_{+1}(+500^{\text{ps}})\rangle = +8$. The decrement in the mode purity with increment in the topological charge can be attributed to the more pronounced effect of azimuthal discretization as the azimuthal phase variations become more rapid. It should be remarked that the mode purity enhances significantly by minimizing the undesired frequency mixing products which is shown in section S4 of the Supplementary Material.

On the other hand, the results in Figure 6i show two linearly time-varying trajectories with opposite slopes and one time-variant trajectory which point toward dominant generation of two dynamic beams with time-varying OAM states of $|l_{\pm 1}(t)\rangle = |\pm 16\Delta f t\rangle$ and a static beam with a fixed OAM state of $|l_0\rangle = |0\rangle$. While the dynamic beams are attributed to the coherent space-time path in the interference between up-modulated and down-modulated frequency harmonics, the static beam is due to coherent interference of imperfectly supressed fundamental frequency harmonics as shown in the output spectrum in Figure 5d. The presence of this static beam as well as other vortices resulting from undesirable higher-order frequency harmonics are the main underlying reasons to the perturbation of time-domain near-field profile and the lack of mode purity compared to ideal optical vortices as discussed in section S4 of the Supplementary Material. The normalized spatial mode purities of dynamic beams in this case are symmetric with respect to $t = 0$ within the time interval of $|t| < 0.5$ns due to time-reversal symmetry of the rectangle-like modulation waveform. Nevertheless, they are not symmetric in the Hilbert space with respect to $|l\rangle = 0$ as a result of broken azimuthal symmetry of the frequency gradient TMM (increase in the modulation frequency by increment in the azimuthal angle). Specifically, the normalized spatial mode purities of dynamic beams in this case increase from 49.12 and 17.75% at $|l_{+1}(-500^{\text{ps}})\rangle = -8$ and $|l_{-1}(-500^{\text{ps}})\rangle = +8$, respectively to 99.94% at the state of $|l_{\pm 1}(0^{\text{ps}})\rangle = 0$ and then decrease to 17.75 and 49.12% at $|l_{+1}(+500^{\text{ps}})\rangle = +8$ and $|l_{-1}(+500^{\text{ps}})\rangle = -8$, respectively (more details on the efficiency and mode purity are provided in section S4 of the Supplementary Material).

It should be remarked that although the reflected light is decomposed into integer OAM states forming an orthogonal basis, according to the given theoretical formulation, the topological charge of generated dynamic twisted light beams varies continuously and linearly as a function of time ($l = N\Delta f t$) yielding fractional or non-

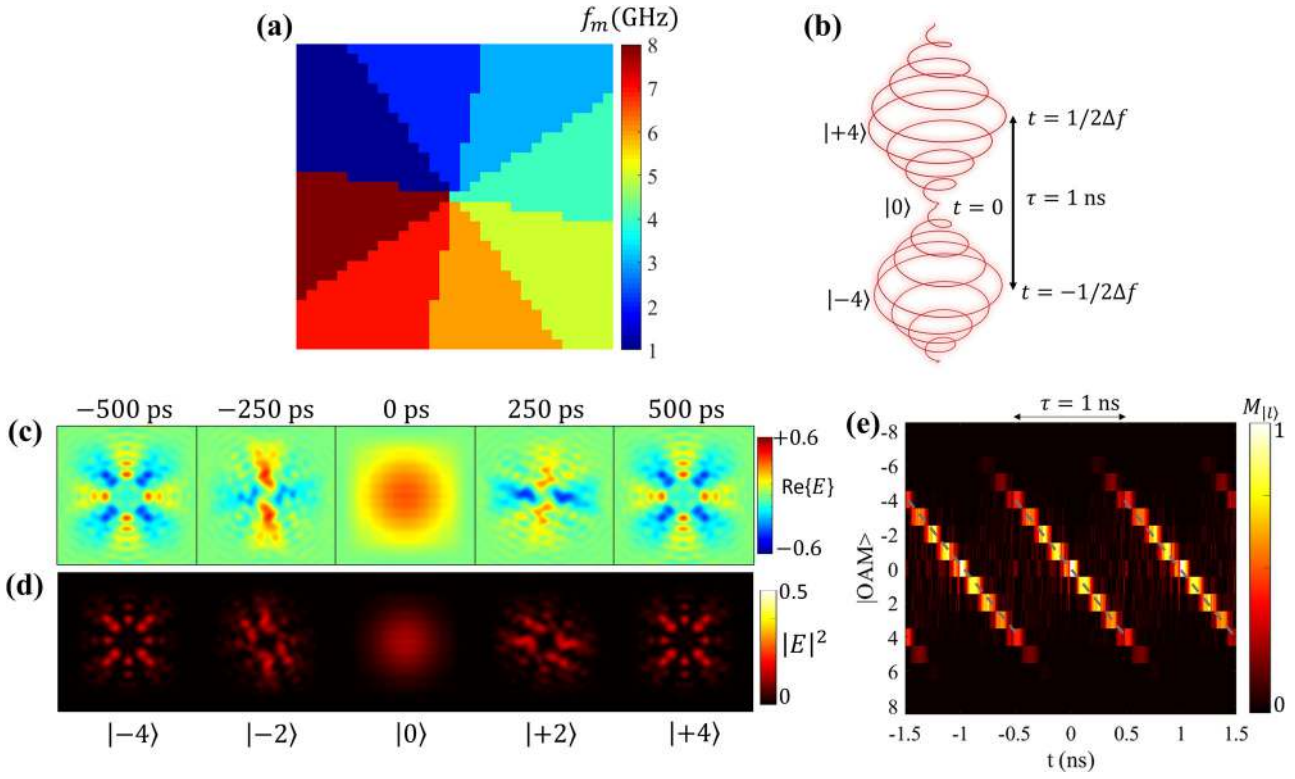


**Figure 7:** **(a)** The spatial distribution of modulation frequency across the metasurface aperture. **(b)** The schematic depiction of temporal evolution of the dynamic twisted light beam generated by the frequency gradient TMM biased with the sawtooth-like waveform. The calculated **(c)** real part and **(d)** intensity of the reflected electric field from the frequency gradient TMM biased with sawtooth-like waveform across the transverse x-y plane at a distance of $2\lambda_0$ above the metasurface at different instant of times within time-interval of $T = 1$ ns in the steady-state.**(e)** The normalized spatial mode purity of the reflected light from azimuthally divided frequency gradient TMM calculated as functions of OAM state and time.

integer values. The phase of fractional optical vortices could be mathematically expressed as $\exp(iX\varphi)$ wherein in contrary to conventional optical vortices, $X$ is not necessarily an integer number (i.e., $X \in \mathbb{Q}$). Since these kinds of structured lights correspond to multi-dimensional vector states residing in the OAM Hilbert space, they have been exploited to reveal the high-dimensional quantum property of an entangled system as well as optical micromanipulation [95].

While the nearfield profiles of time-domain reflected field are perturbed by the coexistence of parasitic vortices due to undesired frequency mixing products, the optical responses of the frequency gradient TMM in both cases are dominated by the self-torqued time-varying optical vortices with topological charges of $l_{\pm1}(t)$ whose time-varying OAM and torque can be calculated as $\mathbf{L}_p(t) = \pm 16\hbar\,\Delta f\,t$ and $\tau_{\pm1} = \pm 16\hbar\Delta f$. The angular acceleration in the twisted light fields generated by TMMs and the degree of their self-torque can be simply controlled by adjusting the frequency offset between different azimuthal sections of the metasurface ($\Delta f$). Moreover, adjusting the azimuthal frequency gradient profile can yield control over the upper and lower bounds of temporal variations in the topological charge. To illustrate such a capability, we imprint an azimuthally linear frequency gradient as $f_m(\varphi) = 8(\varphi/2\pi)\Delta f$ across the TMM via biasing each two adjacent azimuthal sections with the same modulation frequency as shown in Figure 7a. Adopting the sawtooth-like modulation waveform yields generation of a dominant dynamic optical vortex whose topological charge is varying in the range of $-4 \le l_{+1}(t) \le +4$ within time intervals of $T = 1/\Delta f$ at the steady-state whose intensity is schematically illustrated in Figure 7b. Figure 7c,d demonstrate the calculated real-part and intensity of the reflected electric field from the TMM, respectively across the transverse x-y plane at a distance of $2\lambda_0$ at different instants of time within temporal periodicity cycle of $-1/2\Delta f \le t \le 1/2\Delta f$. The results clearly show the evolution of OAM state of the optical vortex from $|-4\rangle$ at $t = -1/2\Delta f$ to $|0\rangle$ at $t = 0$ with a decrease in the radius of vortex, followed by an increase in the

radius associate by evolution of OAM state of $|0\rangle$ at $t = 0$ to $|+4\rangle$ at $t = 1/2\Delta f$. The temporal evolution of this twisted light beam is also visualized in the Supplementary Movie 3. The normalized spatial mode purity of the reflected light from the TMM is plotted in Figure 7e as a function of time, verifying the linear dependency of topological charge on time as $l(t) = 4\Delta f t$. The mode purity in this case increases from 41.49% at $|l_{+1}(-500^{ps})\rangle = -4$ to 99.94% at $|l_{+1}(0^{ps})\rangle = 0$ and eventually decreases to 41.49% for the topological charge of $|l_{+1}(+500^{ps})\rangle = +4$ (for more details regarding the mode purity of other states, please refer to section S4 of the Supplementary Material). The self-torque acting on the dominant time-varying optical vortex in this light beam can be quantified as $\tau = 4\hbar\Delta f$.

The results presented in this section clearly illustrate the capability of TMMs with azimuthal frequency gradient to generate time-varying optical vortices possessing self-torque whose evolution and diversity can be flexibility controlled by tuning the frequency gradient profile and modulation waveform.

# 5 Conclusions

In this paper, we have established a novel paradigm for generation of dynamic twisted light beams with time-varying OAM via time-modulated metasurfaces with azimuthal frequency gradient. The topological charge of these structure light beams varies continuously and periodically at the steady-state with a linear dependence on time and the modulation frequency offset between azimuthal sections of the metasurface, which yields a self-torqued light beam. As a proof-of-concept, we considered an ITO-integrated GMRM consisting of nanodisk heterostructures configured as a dual-gated field effect modulator. The metasurface is azimuthally divided into several subsections wherein the nanodisks are interconnected via biasing lines which are terminated at the edges of each section. This configuration enables addressing each section independently via an RF biasing signal with a different modulation frequency, thus allowing for imprinting an azimuthal frequency gradient on the metasurface. We verified the capability of the proposed metasurface platform for generation of time-varying optical vortices and theoretically demonstrated its flexibility in tuning the degree of self-torque and temporal evolution of the beams by exploring the role of modulation waveform and azimuthal frequency gradient profile. The concepts and the results presented in this paper point toward a route for generating a new class of structured light beams for time-division multiple access in optical and quantum communications as well as unprecedented optomechanical manipulation.

**Acknowledgments:** This work was supported in part by the US Air Force Office of Scientific Research (AFOSR), FA9550-18-1-0354.

**Author contribution:** All the authors have accepted responsibility for the entire content of this submitted manuscript and approved submission.

**Research funding:** This research was funded by the US Air Force Office of Scientific Research (AFOSR), FA9550-18-1-0354.

**Conflict of interest statement:** The authors declare no conflicts of interest regarding this article.

# References

[1] R. A. Beth, "Mechanical detection and measurement of the angular momentum of light," *Phys. Rev.*, vol. 50, no. 2, pp. 115, 1936.

[2] Y. Shen, X. Wang, Z. Xie, et al., "Optical vortices 30 years on: OAM manipulation from topological charge to multiple singularities," *Light Sci. Applic.*, vol. 8, pp. 1–29, 2019.

[3] J. Wang, J.-Y. Yang, I. M. Fazal, et al., "Terabit free-space data transmission employing orbital angular momentum multiplexing," *Nat. Photonics*, vol. 6, pp. 488, 2012.

[4] N. Bozinovic, Y. Yue, Y. Ren, et al., "Terabit-scale orbital angular momentum mode division multiplexing in fibers," *Science*, vol. 340, pp. 1545–1548, 2013.

[5] K. Gahagan, and G. Swartzlander, "Optical vortex trapping of particles," *Opt. Lett.*, vol. 21, pp. 827–829, 1996.

[6] M. Padgett, and R. Bowman, "Tweezers with a twist," *Nat. Photonics*, vol. 5, p. 343, 2011.

[7] J. H. Lee, G. Foo, E. G. Johnson, and G. A. Swartzlander, Jr, "Experimental verification of an optical vortex coronagraph," *Phys. Rev. Lett.*, vol. 97, 2006, Art no. 053901.

[8] L. Li, and F. Li, "Beating the Rayleigh limit: Orbital-angular-momentum-based superresolution diffraction tomography," *Phys. Rev. E*, vol. 88, 2013, Art no. 033205.

[9] A. Mair, A. Vaziri, G. Weihs, and A. Zeilinger, "Entanglement of the orbital angular momentum states of photons," *Nature*, vol. 412, p. 313, 2001.

[10] G. Molina-Terriza, A. Vaziri, R. Ursin, and A. Zeilinger, "Experimental quantum coin tossing," *Phys. Rev. Lett.*, vol. 94, 2005, Art no. 040501.

[11] X. Wang, Z. Nie, Y. Liang, J. Wang, T. Li, and B. Jia, "Recent advances on optical vortex generation," *Nanophotonics*, vol. 7, pp. 1533–1556, 2018.

[12] M. Beijersbergen, R. Coerwinkel, M. Kristensen, and J. Woerdman, "Helical-wavefront laser beams produced with a spiral phaseplate," *Opt. Commun.*, vol. 112, pp. 321–327, 1994.

[13] H. Li, D. B. Phillips, X. Wang, et al., "Orbital angular momentum vertical-cavity surface-emitting lasers," *Optica*, vol. 2, no. 6, pp. 547–552, 2015.

[14] X. Hui, S. Zheng, Y. Hu, et al., "Ultralow reflectivity spiral phase plate for generation of millimeter-wave OAM beam," *IEEE Ant. Wireless Propag. Lett.*, vol. 14, pp. 966–969, 2015.

[15] N. Zhou, S. Zheng, X. Cao, et al., "Generating and synthesizing ultrabroadband twisted light using a compact silicon chip," *Opt. Lett.*, vol. 43, no. 13, pp. 3140–3143, 2018.
[16] A. Liu, C. L. Zou, X. Ren, Q. Wang, and G. C. Guo, "On-chip generation and control of the vortex beam," *Appl. Phys. Lett.*, vol. 108, no. 18, 2016, Art no. 181103.
[17] X. Cai, J. Wang, M. J. Strain, et al., "Integrated compact optical vortex beam emitters," *Science*, vol. 338, no. 6105, pp. 363–366, 2012.
[18] A. Mock, D. Sounas, and A. Alù, "Tunable orbital angular momentum radiation from angular-momentum-biased microcavities," *Phys. Rev. Lett.*, vol. 121, no. 10, 2018, Art no. 103901.
[19] S. Zheng, and J. Wang, "On-chip orbital angular momentum modes generator and (de) multiplexer based on trench silicon waveguides," *Opt. Express*, vol. 25, no. 15, pp. 18492–18501, 2017.
[20] R. Feng, J. Yi, S. N. Burokur, L. Kang, H. Zhang, and D. H. Werner, "Orbital angular momentum generation method based on transformation electromagnetics," *Opt. Express*, vol. 26, no. 9, pp. 11708–11717, 2018.
[21] L. Allen, M. W. Beijersbergen, R. J. C. Spreeuw, and J. P. Woerdman, "Orbital angular momentum of light and the transformation of Laguerre-Gaussian laser modes," *Phys. Rev. A*, vol. 45, no. 11, 1992, Art no. 8185.
[22] N. Jhajj, I. Larkin, E. W. Rosenthal, S. Zahedpour, J. K. Wahlstrand, and H. M. Milchberg, "Spatiotemporal optical vortices," *Phys. Rev. X*, vol. 6, no. 3, 2016, Art no. 031037.
[23] K. Y. Bliokh, and F. Nori, "Spatiotemporal vortex beams and angular momentum," *Phys. Rev. A*, vol. 86, no. 3, Art no. 033824, 2012, https://doi.org/10.1103/physreva.86.033824.
[24] I. P. Ivanov, "Colliding particles carrying nonzero orbital angular momentum," *Phys. Rev. D*, vol. 83, no. 9, Art no. 093001, 2011, https://doi.org/10.1103/physrevd.83.093001.
[25] J. Leach, A. J. Wright, J. B. Götte, et al., ""Aether drag" and moving images," *Phys. Rev. Lett.*, vol. 100, no. 15, Art no. 153902, 2008. https://doi.org/10.1103/physrevlett.100.153902.
[26] S. Franke-Arnold, G. Gibson, R. W. Boyd, and M. J. Padgett, "Rotary photon drag enhanced by a slow-light medium," *Science*, vol. 333, no. 6038, pp. 65–67, 2011.
[27] P. Villoresi, T. Jennewein, F. Tamburini, et al., "Experimental verification of the feasibility of a quantum channel between space and Earth," *New J. Phys.*, vol. 10, no. 3, Art no. 033038, 2008. https://doi.org/10.1088/1367-2630/10/3/033038.
[28] C. Schulze, F. S. Roux, A. Dudley, R. Rop, M. Duparré, and A. Forbes, "Accelerated rotation with orbital angular momentum modes," *Phys. Rev. A*, vol. 91, no. 4, Art no. 043821, 2015, https://doi.org/10.1103/physreva.91.043821.
[29] A. H. Dorrah, M. Zamboni-Rached, and M. Mojahedi, "Controlling the topological charge of twisted light beams with propagation," *Phys. Rev. A*, vol. 93, no. 6, Art no. 063864, 2016.
[30] J. Webster, C. Rosales-Guzmán, and A. Forbes, "Radially dependent angular acceleration of twisted light," *Opt. Lett.*, vol. 42, no. 4, pp. 675–678, 2017.
[31] L. Rego, K. M. Dorney, N. J. Brooks, et al., "Generation of extreme-ultraviolet beams with time-varying orbital angular momentum," *Science*, vol. 364, no. 6447, 2019, Art no. eaaw9486.
[32] A. T. O'Neil, and M. J. Padgett, "Three-dimensional optical confinement of micron-sized metal particles and the decoupling of the spin and orbital angular momentum within an optical spanner," *Opt. Commun.*, vol. 185, nos. 1–3, pp. 139–143, 2000.
[33] D. M. Villeneuve, S. A. Aseyev, P. Dietrich, M. Spanner, M. Y. Ivanov, and P. B. Corkum, "Forced molecular rotation in an optical centrifuge," *Phys. Rev. Lett.*, vol. 85, no. 3, 2000, Art no. 542.
[34] M. E. J. Friese, H. Rubinsztein-Dunlop, J. Gold, P. Hagberg, and D. Hanstorp, "Optically driven micromachine elements," *Appl. Phys. Lett.*, vol. 78, no. 4, pp. 547–549, 2001.
[35] M. A. Porras, "Attosecond helical pulses," *Phys. Rev. A*, vol. 100, no. 3, 2019, Art no. 033826.
[36] E. M. Wright, J. Arlt, and K. Dholakia, "Toroidal optical dipole traps for atomic Bose-Einstein condensates using Laguerre-Gaussian beams," *Phys. Rev. A*, vol. 63, no. 1, 2000, Art no. 013608.
[37] N. Yu, and F. Capasso, "Flat optics with designer metasurfaces," *Nat. Mater.*, vol. 13, p. 139, 2014.
[38] H.-H. Hsiao, C. H. Chu, and D. P. Tsai, "Fundamentals and applications of metasurfaces," *Small Methods*, vol. 1, 2017, Art no. 1600064.
[39] S. Kruk, F. Ferreira, N. Mac Suibhne, et al., "Transparent dielectric metasurfaces for spatial mode multiplexing," *Laser Photonics Rev.*, vol. 12, 2018, Art no. 1800031.
[40] E. Nazemosadat, M. Mazur, S. Kruk, et al., "Dielectric broadband metasurfaces for fiber mode-multiplexed communications," *Adv. Opt. Mater.*, vol. 7, no. 14, 2019, Art no. 1801679.
[41] Y. Shuang, H. Zhao, W. Ji, T. J. Cui, and L. Li, "Programmable high-order OAM-carrying beams for direct-modulation wireless communications," *IEEE J. Emerg. Select. Top. Circuits Syst.*, vol. 10, no. 1, pp. 29–37, 2020.
[42] T. Cui, B. Bai, and H. B. Sun, "Tunable metasurfaces based on active materials," *Adv. Funct. Mater.*, vol. 29, no. 10, 2019, Art no. 1806692.
[43] L. Kang, R. P. Jenkins, and D. H. Werner, "Recent progress in active optical metasurfaces," *Adv. Opt. Mater.*, vol. 7, no. 14, 2019, Art no. 1801813.
[44] Q. He, S. Sun, and L. Zhou, "Tunable/reconfigurable metasurfaces: physics and applications," *Research*, vol. 2019, 2019, Art no. 1849272.
[45] A. M. Shaltout, V. M. Shalaev, and M. L. Brongersma, "Spatiotemporal light control with active metasurfaces," *Science*, vol. 364, 2019, Art no. eaat3100.
[46] C. Elachi, *Electromagnetic Wave Propagation and Source Radiation in Space-Time Periodic Media (No. TR-61)*, Pasadena, CA, USA, CALIFORNIA INST OF TECH PASADENA ANTENNA LAB, 1971.
[47] S. Taravati, and A. A. Kishk, "Space-Time Modulation: Principles and Applications," *IEEE Microw. Mag.*, vol. 21, no. 4, pp. 30–56, 2020.
[48] C. Caloz, and Z. L. Deck-Léger, "Spacetime metamaterials, part I: General concepts," *IEEE Trans. Antennas Propag.*, vol. 68, no. 3, pp. 1569–1582, 2020.
[49] C. Caloz, and Z. L. Deck-Léger, "Spacetime metamaterials, Part II: Theory and applications," *IEEE Trans. Antennas Propag.*, vol. 68, no. 3, pp. 1583–1598, 2020.
[50] A. Shaltout, A. Kildishev, and V. Shalaev, "Time-varying metasurfaces and Lorentz non-reciprocity," *Opt. Mater. Express*, vol. 5, no. 11, pp. 2459–2467, 2015.
[51] Y. Hadad, D. L. Sounas, and A. Alu, "Space-time gradient metasurfaces," *Phys. Rev. B*, vol. 92, no. 10, 2015, Art no. 100304.
[52] Y. Shi, S. Han, and S. Fan, "Optical circulation and isolation based on indirect photonic transitions of guided resonance modes," *ACS Photonics*, vol. 4, no. 7, pp. 1639–1645, 2017.

[53] S. Taravati, and G. V. Eleftheriades, *Full-Duplex Nonreciprocal-Beam-Steering Metasurfaces Comprising Time-Modulated Twin Meta-Atoms*, 2019. arXiv preprint arXiv:1911.04033.
[54] X. Wang, A. Diaz-Rubio, H. Li, S. A. Tretyakov, and A. Alu, "Multifunctional Space-Time Metasurfaces," *Phys. Rev. Appl*, vol. 13, 2020, Art no. 044040.
[55] M. M. Salary, S. Jafar-Zanjani, and H. Mosallaei, "Nonreciprocal optical links based on time-modulated nanoantenna arrays: Full-duplex communication," *Phys. Rev. B*, vol. 99, no. 4, Art no. 045416, 2019, https://doi.org/10.1103/physrevb.99.045416.
[56] L. Zhang, X. Q. Chen, S. Liu, et al., "Space-time-coding digital metasurfaces," *Nat. Commun.*, vol. 9, no. 1, pp. 1–11, 2018.
[57] L. Zhang, X. Q. Chen, R. W. Shao, et al., "Breaking reciprocity with space-time-coding digital metasurfaces," *Adv. Mater.*, vol. 31, no. 41, 2019, Art no. 1904069.
[58] J. Zhao, X. Yang, J. Y. Dai, et al., "Programmable time-domain digital-coding metasurface for non-linear harmonic manipulation and new wireless communication systems," *Nat. Sci. Rev.*, vol. 6, no. 2, pp. 231–238, 2019.
[59] H. Rajabalipanah, A. Abdolali, and K. Rouhi, "Reprogrammable Spatiotemporally Modulated Graphene-Based Functional Metasurfaces," *IEEE J. Emerg. Select. Top. Circuits Syst.*, vol. 10, no. 1, pp. 75–87, 2020.
[60] J. Zang, D. Correas-Serrano, J. Do, X. Liu, A. Alvarez-Melcon, and J. Gomez-Diaz, "Nonreciprocal Wavefront Engineering with Time-Modulated Gradient Metasurfaces," *Phys. Rev. Appl.*, vol. 11, 2019, Art no. 054054.
[61] M. M. Salary, S. Jafar-Zanjani, and H. Mosallaei, "Electrically tunable harmonics in time-modulated metasurfaces for wavefront engineering," *New J. Phys.*, vol. 20, no. 12, 2018, Art no. 123023
[62] M. Liu, D. A. Powell, Y. Zarate, and I. V. Shadrivov, "Huygens' metadevices for parametric waves," *Phys. Rev. X*, vol. 8, Art no. 031077, 2018, https://doi.org/10.1103/physrevx.8.031077.
[63] M. M. Salary, S. Jafar-Zanjani, and H. Mosallaei, "Time-varying metamaterials based on graphene-wrapped microwires: modeling and potential applications," *Phys. Rev. B*, vol. 97, no. 11, Art no. 115421, 2018, https://doi.org/10.1103/physrevb.97.115421.
[64] M. S. Mirmoosa, G. A. Ptitcyn, V. S. Asadchy, and S. A. Tretyakov, "Time-varying reactive elements for extreme accumulation of electromagnetic energy," *Phys. Rev. Appl.*, vol. 11, no. 1, Art no. 014024, 2019, https://doi.org/10.1103/physrevapplied.11.014024.
[65] M. Liu, A. B. Kozyrev, and I. V. Shadrivov, "Time-varying metasurfaces for broadband spectral camouflage," *Phys. Rev. Appl.*, vol. 12, no. 5, Art no. 054052, 2019, https://doi.org/10.1103/physrevapplied.12.054052.
[66] X. Wang, and C. Caloz, *Spread-Spectrum Selective Camouflaging Based on Time-Modulated Metasurface*, 2019. arXiv preprint arXiv:1909.04480.
[67] A. Shlivinski, and Y. Hadad, "Beyond the bode-fano bound: Wideband impedance matching for short pulses using temporal switching of transmission-line parameters," *Phys. Rev. Lett.*, vol. 121, no. 20, Art no. 204301, 2018, https://doi.org/10.1103/physrevlett.121.204301.
[68] H. Li, A. Mekawy, and A. Alù, "Beyond Chu's Limit with Floquet Impedance Matching," *Phys. Rev. Lett.*, vol. 123, no. 16, Art no. 164102, 2019, https://doi.org/10.1103/physrevlett.123.164102.
[69] E. Galiffi, P. A. Huidobro, and J. B. Pendry, "Broadband nonreciprocal amplification in luminal metamaterials," *Phys. Rev. Lett.*, vol. 123, no. 20, Art no. 206101, 2019, https://doi.org/10.1103/physrevlett.123.206101.
[70] Y. Sivan, and J. B. Pendry, "Time reversal in dynamically tuned zero-gap periodic systems," *Phys. Rev. Lett.*, vol. 106, no. 19, Art no. 193902, 2011, https://doi.org/10.1103/physrevlett.106.193902.
[71] N. Chamanara, and C. Caloz, *Linear Pulse Compansion Using Co-propagating Space-Time Modulation*, 2018. arXiv preprint arXiv:1810.04129.
[72] N. Chamanara, Y. Vahabzadeh, and C. Caloz, "Simultaneous control of the spatial and temporal spectra of light with space-time varying metasurfaces," *IEEE Trans. Antennas Propag.*, vol. 67, no. 4, pp. 2430–2441, 2019.
[73] M. M. Salary, and H. Mosallaei, "Time-modulated conducting oxide metasurfaces for adaptive multiple access optical communication," *IEEE Trans. Antennas Propag.*, vol. 68, no. 3, pp. 1628–1642, 2020.
[74] H. Barati Sedeh, M. M. Salary, and H. Mosallaei, "Topological space-time photonic transitions in angular-momentum-biased metasurfaces," *Adv. Opt. Mater.*, vol. 8, no. 11, 2020, Art no. 2000075.
[75] S. Inampudi, M. M. Salary, S. Jafar-Zanjani, and H. Mosallaei, "Rigorous space-time coupled-wave analysis for patterned surfaces with temporal permittivity modulation," *Opt. Mater. Express*, vol. 9, no. 1, pp. 162–182, 2019.
[76] M. M. Salary, S. Farazi, and H. Mosallaei, "A dynamically modulated all-dielectric metasurface doublet for directional harmonic generation and manipulation in transmission," *Adv. Opt. Mater.*, vol. 7, no. 23, 2019, Art no. 1900843.
[77] P. Antonik, M. C. Wicks, H. D. Griffiths, and C. J. Baker, "Frequency diverse array radars," in *2006 IEEE Conference on Radar*, Verona, NY, USA, IEEE, 2006, p. 3. April.
[78] P. F. Sammartino, C. J. Baker, and H. D. Griffiths, "Frequency diverse MIMO techniques for radar," *IEEE Trans. Aerospace Electron. Syst.*, vol. 49, no. 1, pp. 201–222, 2013.
[79] A. M. Shaltout, K. G. Lagoudakis, J. van de Groep, et al., "Spatiotemporal light control with frequency-gradient metasurfaces," *Science*, vol. 365, no. 6451, pp. 374–377, 2019.
[80] Z. Wu, and A. Grbic, "Serrodyne frequency translation using time-modulated metasurfaces," *IEEE Trans. Antennas Propag.*, vol. 68, no. 3, pp. 1599–1606, 2020.
[81] D. Ramaccia, D. L. Sounas, A. Alu, A. Toscano, and F. Bilotti, "Phase-induced frequency conversion and doppler effect with time-modulated metasurfaces," *IEEE Trans. Antennas Propag.*, vol. 68, no. 3, pp. 1607–1617, 2019.
[82] K. Yamada, K. Asai, Y. H. Ko, et al., "High reflectance with steep reflection phase spectrum by guided-mode resonance," *Appl. Phys. Express*, vol. 9, no. 12, 2016, Art no. 122501.
[83] G. Kafaie Shirmanesh, R. Sokhoyan, R. A. Pala, and H. A. Atwater, "Dual-gated active metasurface at 1550 nm with wide (> 300°) phase tunability," *Nano Lett.*, vol. 18, no. 5, pp. 2957–2963, 2018.
[84] A. Forouzmand, and H. Mosallaei, "Electro-optical amplitude and phase modulators based on tunable guided-mode resonance effect," *ACS Photonics*, vol. 6, no. 11, pp. 2860–2869, 2019.
[85] V. J. Sorger, N. D. Lanzillotti-Kimura, R.-M. Ma, and X. Zhang, "Ultracompact silicon nanophotonic modulator with broadband response," *Nanophotonics*, vol. 1, no. 1, pp. 17–22, 2012.
[86] V. E. Babicheva, A. Boltasseva, and A. V. Lavrinenko, "Transparent conducting oxides for electro-optical plasmonic modulators," *Nanophotonics*, vol. 4, pp. 165–185, 2015.

[87] A. Howes, W. Wang, I. Kravchenko, and J. Valentine, "Dynamic transmission control based on all-dielectric Huygens metasurfaces," *Optica*, vol. 5, no. 7, pp. 787–792, 2018.
[88] Y. W. Huang, H. W. H. Lee, R. Sokhoyan, et al., "Gate-tunable conducting oxide metasurfaces," *Nano Lett.*, vol. 16, no. 9, pp. 5319–5325, 2016.
[89] J. Park, J.-H. Kang, S. J. Kim, X. Liu, and M. L. Brongersma, "Dynamic reflection phase and polarization control in metasurfaces," *Nano Lett.*, vol. 17, pp. 407–413, 2017.
[90] A. Forouzmand, M. M. Salary, G. K. Shirmanesh, R. Sokhoyan, H. A. Atwater, and H. Mosallaei, "Tunable all-dielectric metasurface for phase modulation of the reflected and transmitted light via permittivity tuning of indium tin oxide," *Nanophotonics*, vol. 8, pp. 415–427, 2019.
[91] M. M. Salary, and H. Mosallaei, "Electrically tunable metamaterials based on multimaterial nanowires incorporating transparent conductive oxides," *Sci. Rep.*, vol. 7, pp. 1–14, 2017.
[92] A. Forouzmand, M. M. Salary, S. Inampudi, and H. Mosallaei, "A tunable multigate Indium-Tin-oxide-assisted all-dielectric metasurface," *Adv. Opt. Mater.*, vol. 6, no. 7, 2018, Art no. 1701275.
[93] J. Hwang, and J. W. Roh, "Electrically tunable two-dimensional metasurfaces at near-infrared wavelengths," *Opt. Express*, vol. 25, pp. 25071–25078, 2017.
[94] T. Kondo, S. Ura, and R. Magnusson, "Design of guided-mode resonance mirrors for short laser cavities," *J. Opt. Soc. Am. A*, vol. 32, no. 8, 2015, Art no. 1454.
[95] S. S. R. Oemrawsingh, X. Ma, D. Voigt, A. Aiello, E. T. Eliel, and J. P. Woerdman, "Experimental demonstration of fractional orbital angular momentum entanglement of two photons," *Phys. Rev. Lett.*, vol. 95, no. 24, 2005, Art no. 240501.

**Supplementary material:** The online version of this article offers supplementary material https://doi.org/10.1515/nanoph-2020-0202.